

Diagnosing Lateral Mixing in the Upper Ocean with Virtual Tracers: Spatial and Temporal Resolution Dependence

SHANE R. KEATING AND K. SHAFER SMITH

*Center for Atmosphere Ocean Science, Courant Institute of Mathematical Sciences, New York University,
New York, New York*

PETER R. KRAMER

Department of Mathematical Sciences, Rensselaer Polytechnic Institute, Troy, New York

(Manuscript received 16 September 2010, in final form 25 February 2011)

ABSTRACT

Several recent studies diagnose lateral stirring and mixing in the upper ocean using altimetry-derived velocity fields to advect “virtual” particles and fields offline. However, the limited spatiotemporal resolution of altimetric maps leads to errors in the inferred diagnostics, because unresolved scales are necessarily imperfectly modeled. The authors examine a range of tracer diagnostics in two models of baroclinic turbulence: the standard Phillips model, in which dispersion is controlled by large-scale eddies, and the Eady model, where dispersion is determined by local scales of motion. These models serve as a useful best- and worst-case comparison and a valuable test of the resolution sensitivity of tracer diagnostics.

The effect of unresolved scales is studied by advecting tracers using model velocity fields subsampled in space and time and comparing the derived tracer diagnostics with their “true” value obtained from the fully resolved flow. The authors find that eddy diffusivity and absolute dispersion, which are governed by large-scale dynamics, are insensitive to spatial sampling error in either flow. Measures that depend strongly on small scales, such as relative dispersion and finite-time Lyapunov exponents, are highly sensitive to spatial sampling in the Eady model. Temporal sampling error is found to have a more complicated behavior because of the onset of particle overshoot leading to scrambling of Lagrangian diagnostics. This leads to a potential restriction on the utility of raw altimetry maps for studying mixing in the upper ocean. The authors conclude that offline diagnostics of mixing in ocean flows with an energized submesoscale should be viewed with some caution.

1. Introduction

The problem of effectively diagnosing and parameterizing eddy processes in oceanic mesoscale turbulence remains a critical limitation upon our ability to accurately model the ocean’s large-scale circulation. Quantifying lateral mixing in the upper ocean in particular is crucial not only for the development of more skillful eddy parameterization schemes but also for the understanding of observed temperature and chlorophyll distributions (Mahadevan and Campbell 2002), pollutant dispersal (Hazell and England 2003), and plankton

dynamics (Martin 2003). However, although valuable data on horizontal dispersion and mixing are provided by in situ observations of surface drifters and controlled tracer release experiments (e.g., LaCasce and Ohlmann 2003; Lumpkin and Elipot 2010), the considerable cost and logistical difficulties of large-scale field observations limit their effectiveness, whereas satellite imagery of sea surface temperature and ocean color (e.g., Abraham et al. 2000; Isern-Fontanet et al. 2006) are currently unable to provide continuous, global monitoring of the ocean surface.

Altimetric measurements of sea surface height (SSH) anomalies, provided by *Jason-1*, Ocean Topography Experiment (TOPEX)/Poseidon, and other satellite missions are now routinely used to estimate geostrophic velocities at the ocean surface (Fu 2010). In recent years, a number of studies have made use of altimetry-derived

Corresponding author address: Shane R. Keating, Courant Institute of Mathematical Sciences, New York University, 251 Mercer St., New York, NY 10012.
E-mail: skeating@cims.nyu.edu

velocity fields to diagnose lateral mixing and transport in the upper ocean on both regional and global scales, using time series of the observed surface flow to advect virtual tracers, from which the relevant Eulerian or Lagrangian diagnostics can be computed. Diagnostics calculated from the trajectories of virtual particles (relative dispersion, finite-time, and finite-scale Lyapunov exponents) have been used to characterize mixing in the Tasman Sea (Abraham and Bowen 2002; Waugh et al. 2006), the Algerian basin (d'Ovidio et al. 2009), the Agulhas Current (Beron-Vera et al. 2008), and the World Ocean (Waugh and Abraham 2008), as well as to examine the role of geostrophic stirring on phytoplankton blooms in the northeast Atlantic (Lehahn et al. 2007) and the interaction between mixing and biological production in eastern Atlantic upwelling zones (Rossi et al. 2008). Similarly, virtual scalar fields have been used to infer diffusivities in the Antarctic Circumpolar Current (Marshall et al. 2006; Shuckburgh et al. 2009a,b).

The velocity fields inferred from satellite altimetry are, however, subject to inevitable inaccuracies due to nonuniform satellite coverage and spatial and temporal sampling resolutions that are strongly limited by the orbital characteristics of the satellite itself, resulting in effective spatial resolutions of about 100 km and temporal resolutions on the order of 10 days. Although gyre-scale, subbasin-scale, and some mesoscale processes can be expected to be captured by this range, the effect of unresolved scales on eddy transport processes has not been fully quantified. The limited resolution of altimetry products allows for model error arising from the fact that an imperfect model is used to represent the effect of the unresolved flow in mixing and transport at larger scales, whether this model is implicit (e.g., the unresolved velocity field is omitted) or explicit (e.g., the effect of the unresolved field on a virtual tracer is modeled as an eddy diffusivity).

The transport properties of a turbulent flow can be significantly altered by filtering out motions on fast space and time scales. Bennett (1984) argued that the relative dispersion of balloons in the stratosphere depends sensitively on the slope of the kinetic energy (KE) spectrum and identified two dynamical regimes governing the evolution of advected quantities. For self-similar kinetic energy spectra of the form $E(k) \propto k^{-\alpha}$, where k is the horizontal wavenumber, particle dispersion will be governed by eddies on the energy-containing scale when $\alpha > 3$ (spectrally nonlocal dynamics) and by eddies on the scale of dispersion when $\alpha < 3$ (spectrally local dynamics). This transition from local to nonlocal dynamics is apparent in the scale dependence of the characteristic turbulent time scale,

$$\tau(k) = \left[\int_0^k p^2 E(p) dp \right]^{-1/2}, \quad (1)$$

where k is the magnitude of the horizontal wave vector (Babiano et al. 1985; Shepherd et al. 2000). The time scale τ represents the local distortion time due to the effective mean shear from wavenumbers $p \leq k$ (Kraichnan 1971). For steep kinetic energy spectra with $\alpha > 3$, the integral in (1) is dominated by the large scales (small p) and is effectively independent of the local wavenumber k . In the nonlocal case, then, particle dispersion is controlled by the velocity field at the largest scales, typically the energy-containing scales. Conversely, for sufficiently shallow kinetic energy spectra with $\alpha < 3$, the time scale in (1) is a function of the local horizontal wavenumber and particle dispersion on a given horizontal scale is controlled by the velocity field on that scale. For the marginal case of $\alpha < 3$, the time scale $\tau(k)$ depends only logarithmically on the horizontal wavenumber and particle dispersion is weakly nonlocal.

The distinction between regimes of local and nonlocal spectral dynamics places an important constraint on our ability to diagnose mixing from low-resolution velocity datasets. In particular, the paradigm of chaotic advection is a special case of nonlocal dynamics in which smoothly varying, quasi-periodic velocity fields generate chaotic mixing on small scales (Ottino 1990). Conversely, chaotic advection is inconsistent with local dynamics, suggesting that mixing in this regime is highly sensitive to the spatial and temporal resolution of the velocity field. As such, the reliability of diagnostics of mixing based on low-resolution velocity fields is intrinsically linked to the steepness of the kinetic energy spectrum, a point made independently by Bartello (2000) and Shepherd et al. (2000) in the context of the atmosphere. Motivated by simulations of atmospheric turbulence exhibiting kinetic energy spectra with $\alpha > 3$, $\alpha \approx 3$, and $\alpha < 3$ in the stratosphere, extratropical troposphere, and mesosphere, respectively, these authors concluded that in the stratosphere relatively coarsely resolved winds can be used to accurately advect tracers and Lagrangian particles and consequently that offline diagnostics (tracer variance, correlation times, and Lyapunov exponents) based on the temporal evolution of these fields are fairly reliable measures of mixing in the stratosphere. In contrast, care must be taken in extending these diagnostics to winds in the mesosphere and, to a lesser extent, the extratropical tropopause, because they are likely to be resolution dependent.

Measurements of the submesoscale kinetic energy spectrum of the upper ocean are more limited than in the atmosphere (for a recent review, see Ferrari and Wunsch 2009). Stammer (1997) analyzed midlatitude

sea surface height and surface velocity data from the TOPEX/Poseidon satellite and found a spectral exponent of $\alpha \approx 3$ over the mesoscale–submesoscale range, a result that is apparently consistent with a picture of geostrophic turbulence driven by baroclinic instability (Charney 1971; Salmon 1980; Smith and Vallis 2002). However, calibration error and noise dominate the TOPEX/Poseidon signal on scales smaller than about 100 km, so measurements of power-law exponents from this range should be viewed with caution (Ferrari and Wunsch 2009). More recently, attention has focused on the role of surface trapped modes that act to flatten the kinetic energy spectrum at high wavenumbers. A growing body of evidence suggests that these modes are crucial to the understanding of submesoscale dynamics and transport in the upper ocean: these include drifter trajectories (Lumpkin and Elipot 2010) and more recent satellite measurements (Scott and Wang 2005; Le Traon et al. 2008) as well as high-resolution primitive equation ocean models (Klein et al. 2008). The results of these studies suggest a significantly shallower ($\alpha \approx 2$) kinetic energy spectrum in the mesoscale–submesoscale range, raising important questions about the robustness of altimetry-inferred mixing diagnostics in the upper ocean.

A central goal of this study is to explicitly evaluate the importance of surface trapped modes and other submesoscale dynamics on spatial and temporal resolution sensitivity. To that end, we employ two phenomenological models of quasigeostrophic turbulence: the classical two-layer Phillips model of geostrophic turbulence (Phillips 1954) and the nonlinear Eady model, in which the dynamics is driven by temperature anomalies on upper and lower surfaces bounding a region of constant potential vorticity (Blumen 1978). In each model, kinetic energy is injected at small wavenumber via baroclinic instability. However, the nonlinear (turbulent) dynamics of the two models are quite distinct, with the Eady model exhibiting a kinetic energy spectral exponent of $\alpha = 5/3$ at its surfaces, in contrast to the well-known $\alpha = 3$ forward cascade of the two-layer Phillips model (Blumen 1978; Held et al. 1995; Tulloch and Smith 2009). The Phillips model and the nonlinear Eady model are complementary, highly simplified models of the real ocean exemplifying either nonlocal or local spectral dynamics. As such, they provide a best- and worst-case comparison and serve as a valuable stress test of the sensitivity of altimetry-inferred diagnostics to the unresolved scales.

Our methodology is to subsample the model flow fields at different spatial and temporal resolutions and to then use these subsampled velocities to advect, off-line, virtual particles and fields, from which a suite of widely used Eulerian, Lagrangian, and quasi-Lagrangian

diagnostics of mixing and stirring can be calculated: eddy diffusivity, absolute (single particle) diffusivity, relative (two particle) diffusivity, finite-time Lyapunov exponents (FTLEs), and effective diascalar diffusivity. The range of diagnostics facilitates an intercomparison of their respective sensitivities to sampling resolution in a tightly controlled context, setting the stage for both building theoretical connections between measures of mixing and stirring and for designing strategies to ameliorate errors in their application to sparse observations of the underlying turbulent flow.

This approach is similar to that of the studies by Bartello (2000) and Shepherd et al. (2000) in the context of atmospheric mesoscale mixing. Likewise, a number of previous studies have examined the reliability of diagnostics inferred from altimetry in regional contexts: Beron-Vera et al. (2008) tested calculations of FTLEs in the South Atlantic using satellite-tracked drifter data; Rossi et al. (2008) tested the sensitivity of FTLEs in a number of eastern Atlantic upwelling zones to observational noise by adding random perturbations of the velocity field at each grid point; and Shuckburgh et al. (2009a) calculated effective diffusivities inferred from virtual tracer experiments in the Southern Ocean and tested their dependence on spatial sampling resolution and the value of the numerical diffusivity. We emphasize that the present study differs from previous analyses of resolution dependence of mixing diagnostics in ocean models (Iudicone et al. 2002; Griffa et al. 2004; Bracco et al. 2004; Poje et al. 2010). These studies typically concentrate on the role of spatial rather than temporal resolution, because the former represents a more costly investment of computational resources. Because both the temporal and spatial resolutions of altimetry products are constrained by orbital considerations, tracer-based diagnostics inferred from satellite altimetry can have nontrivial, overlapping dependencies on the space and time sampling rates: the combined effects of temporal and spatial subsampling are studied here in the same controlled context.

We also show that the estimates of mixing diagnostics from altimetry maps with limited temporal resolution can depend significantly on how the derived velocity fields are used to advect virtual tracers. Two natural approaches are (i) treating the velocity field as piecewise constant in time, changing discontinuously when data become available, and (ii) interpolating the velocity linearly in time between successive times of data acquisition. Because the sampling times are, in practice, not small compared to the relevant time scales of tracer advection, these approaches create differences in the inferred statistical properties of the tracers. Moreover, for the same reason, the inferred mixing diagnostics depend

somewhat on the temporal resolution of the interpolated data, unless the time step is short compared to the tracer advection time scale. These issues are of relevance to the utility of altimetry products such as Archiving, Validation, and Interpretation of Satellite Oceanographic data (AVISO) and the proposed Surface Water Ocean Topography (SWOT) mission.

The paper proceeds as follows: In section 2, we outline and contrast the Phillips and Eady models of quasigeostrophic turbulence. In section 3, we describe a range of diagnostics of mixing and stirring and discuss their properties in both local and nonlocal turbulent flows, whereas in section 4 we examine the dependence of these diagnostics on the spatial and temporal sampling resolutions. We discuss the interplay of spatial and temporal sampling resolution sensitivity as well as temporal interpolation of observations in section 5. Finally, in section 6, we summarize our results.

2. Eddy velocity field models

To study the effects of submesoscale activity on measures of eddy mixing, we generate two synthetic velocity fields that are substantially similar near the deformation scale (the mesoscale) but differ on smaller scales (the submesoscale). The velocity fields are generated from two standard quasigeostrophic models of baroclinic turbulence: the Phillips model (e.g., Phillips 1954; Haidvogel and Held 1980), which is comprised of two immiscible layers, and the Eady model (e.g., Blumen 1978), which advects the buoyancy fields at the upper and lower surfaces and sets the interior potential vorticity to zero. The turbulent dynamics of the two-layer Phillips model are consistent with the predictions of geostrophic turbulence theory (Charney 1971), producing an inverse cascade of kinetic energy in the barotropic mode, with a $-5/3$ kinetic energy spectral slope and a forward potential enstrophy cascade with a steep -3 kinetic energy spectral slope. The turbulent dynamics of the Eady model are similar in the inverse cascade range (above the deformation scale) but differ in the forward cascade. Because the upper and lower surfaces are effectively decoupled at scales below the deformation scale, the forward cascade at the surfaces is determined by conservation of buoyancy variance rather than by conservation of potential enstrophy. This results in a $-5/3$ spectral slope of kinetic energy in the forward cascade near the surfaces.

Given the discussion following (1), we therefore expect that, in the submesoscale range, the Phillips model will exhibit nonlocal spectral dynamics, whereas the Eady model (near the upper surface) will exhibit local spectral dynamics. Because we are primarily interested in the submesoscale (forward cascade) range, we choose

the domain scale, deformation scale, and drag parameters for the two numerical models to give mesoscale eddy fields that have nearly the same energies and horizontal scales and allow only a small inverse cascade. Thus, the eddy scale is only slightly larger than the deformation scale, leaving most of our model resolution available to represent the forward cascade. The details of the models and their numerical implementations are discussed next.

The homogeneous Phillips model on the f plane consists of an advection–diffusion equation for the potential vorticity q_i in each layer and an inversion relation that relates the potential vorticity to the layer-wise streamfunctions ψ_i ,

$$\begin{aligned} \partial_t q_1 + J(\psi_1, q_1) + U \partial_x q_1 + Q_y \partial_x \psi_1 &= D_1, \\ q_1 &= \nabla^2 \psi_1 + \frac{1}{2} k_D^2 (\psi_2 - \psi_1), \\ \partial_t q_2 + J(\psi_2, q_2) - U \partial_x q_2 - Q_y \partial_x \psi_2 &= D_2, \\ q_2 &= \nabla^2 \psi_2 - \frac{1}{2} k_D^2 (\psi_2 - \psi_1), \end{aligned} \quad (2)$$

where U is the baroclinic shear velocity, $Q_y = k_D^2 U$ is the upper-level gradient of the mean potential vorticity, and $k_D = 2\pi f/NH$ is the deformation wavenumber associated with Coriolis parameter f , buoyancy frequency N , and fluid depth H . The term D_i represents dissipation of potential vorticity on small scales (via an exponential filter with high-wavenumber cutoff) and on large scales (via an Ekman drag term).

The Eady model consists of advection–diffusion equations for the buoyancy fields b_i on the upper and lower surfaces,

$$\begin{aligned} \partial_t b_1 + J(\psi_1, b_1) + U \partial_x b_1 - B_y \partial_x \psi_1 &= D_1, \\ \partial_t b_2 + J(\psi_2, b_2) - U \partial_x b_2 - B_y \partial_x \psi_2 &= D_2, \\ (\nabla^2 + f^2/N^2 \partial_z^2) \psi &= 0, \quad b_1 = f_0 \partial_z \psi|_1, \quad b_2 = f_0 \partial_z \psi|_2, \end{aligned} \quad (3)$$

where $B_y = 2fU/H$ is the imposed mean buoyancy gradient on the upper and lower surfaces. The streamfunction is found by setting to zero the three-dimensional quasigeostrophic potential vorticity $q = \nabla^2 \psi + \partial_z (f^2/N^2 \partial_z \psi)$ and solving this homogeneous elliptic problem with boundary conditions given by the buoyancy field on each surface. When the buoyancy frequency N is constant, this inversion can be computed analytically (see, e.g., Tulloch and Smith 2009).

In the Eady model, the quadratic invariants are the total depth-integrated energy density, which is proportional to $\langle \psi b_1 - \psi_2 b_2 \rangle$, and the buoyancy variance on each surface $\langle b_i^2 \rangle$, which are each proportional to the kinetic energy density on its respective surface. This can be contrasted to the two-layer case, in which the

TABLE 1. Model parameters.

Model parameter	Phillips model	Eady model
Domain scale L_0	1024 km	1024 km
Domain depth H	0.878 km	0.878 km
Deformation wavelength L_D	85.3 km	85.3 km
Eddy scale L_E	256 km	256 km
Coriolis parameter f	$1.03 \times 10^{-4} \text{ s}^{-1}$	$1.03 \times 10^{-4} \text{ s}^{-1}$
Buoyancy frequency N	0.01 s^{-1}	0.01 s^{-1}
Baroclinic shear velocity U	0.82 cm s^{-1}	0.15 cm s^{-1}
rms eddy velocity u_{rms}	10.82 cm s^{-1}	2.44 cm s^{-1}
Eddy turn-over time T_{to}	15.2 days	15.1 days

quadratic invariants of the system are (potential) enstrophy $\langle q^2 \rangle$ and energy $-\langle \psi q \rangle$. In both models, baroclinic instability stirs the fluid at approximately the deformation wavenumber, and the injected energy cascades to larger scale, where it is removed by Ekman drag. On the other hand, in the two-layer model, potential enstrophy cascades to smaller scale, whereas in the Eady model it is buoyancy variance (near the surfaces) that cascades to smaller scale. Scaling analysis yields a $k^{-5/3}$ surface kinetic spectrum in the forward cascade (Blumen 1978; Pierrehumbert et al. 1994; Held et al. 1995). Thus, the submesoscale spectral dynamics of the Eady model will be local, and we expect tracer mixing to be controlled by the local scale and therefore strongly dependent on the sampling resolution of the velocity field.

The Phillips and Eady model equations in (2) and (3) were simulated in a doubly periodic domain using a pseudospectral solver with a horizontal grid scale of $1 \text{ km} \times 1 \text{ km}$ in each layer. In each simulation, the domain was $1024 \text{ km} \times 1024 \text{ km} \times 0.88 \text{ km}$. The model parameters H , f , and N (listed in Table 1) were chosen to give a deformation wavelength of $L_D \approx 85 \text{ km}$, relevant to midlatitude open-ocean eddies. In both the Phillips and Eady models, the imposed shear across the two layers excites baroclinic instability that transfers energy to the deformation scale k_D^{-1} , which then cascades to larger scales, where it is removed via Ekman drag. As discussed above, the drag and domain scales are chosen to suppress the inverse cascade and yield eddy fields that have scales only slightly larger than the deformation scale. For the Phillips model, a symmetric top and bottom Ekman drag (Arbic 2000) was used, which, although unrealistic, has the benefit of halting the inverse cascade of energy at some eddy scale $L_E = 256 \text{ km}$ (here defined as the peak in the kinetic energy spectrum) in the absence a gradient in the planetary vorticity (Held and Larichev 1996; Lapeyre and Held 2003; Thompson and Young 2006). The Eady model was found to be somewhat more sensitive to the drag term, so only a weak bottom drag was needed to arrest the cascade at the eddy scale $L_E = 256 \text{ km}$ (see Fig. 1). The forward cascades in each model are absorbed by an

exponential cut-off dissipation that ensures that the flow is smooth at the grid scale. For more details of the numerical representation of the nonlinear Eady model, see Tulloch and Smith (2009).

The upper-level kinetic energy spectra and surface vorticity probability density functions (PDFs) for the two central simulations are shown in Fig. 1. The spectra are nearly identical for scales near the deformation scale and larger (note that, consistent with our design, the inverse cascade subrange between the deformation wavenumber k_D and the spectral peak k_E is quite small) but diverge completely at smaller scales. As predicted, the Phillips model exhibits a steep spectrum (actually somewhat steeper than k^{-3}), whereas the Eady model spectrum is much more energetic, with an approximately $k^{-5/3}$ spectrum in the submesoscale range. Likewise, the surface vorticity PDFs for the two models illustrate that the Eady model possesses a highly energized submesoscale range with strongly non-Gaussian surface vorticity tails. The transition in the Phillips model from a steep kinetic energy spectrum at small scales to a shallow spectrum at large scales suggests that the submesoscale spectral dynamics in this model will be nonlocal and tracer mixing will be controlled by scales on the order of k_D^{-1} and larger. In contrast, the submesoscale spectral dynamics of the Eady model will be local, and we expect tracer mixing to be controlled by the local scale and therefore strongly dependent on the sampling resolution of the velocity field.

3. Tracer mixing in local and nonlocal turbulent flows

Broadly speaking, diagnostics of mixing calculated using altimetric datasets can be categorized as Eulerian, Lagrangian, or quasi Lagrangian. In the Eulerian framework, the mixing and transport properties of the flow are characterized by the temporal evolution of a passively advected scalar field at a fixed point, such as a single moored buoy or a grid point. The general form of the advection–diffusion equation for a scalar concentration $C(\mathbf{x}, t)$ is

$$\frac{\partial C}{\partial t} + \mathbf{u} \cdot \nabla C = \kappa \nabla^2 C + S, \quad C(\mathbf{x}, t_0) = C_0(\mathbf{x}), \quad (4)$$

where S represents the combined effect of sources and sinks of the tracer concentration and κ is the molecular diffusivity. The advection–diffusion equation in (4) is augmented by the initial distribution $C_0(\mathbf{x})$ and solved here using a pseudospectral scheme. The most widely used Eulerian diagnostic is the eddy diffusivity, wherein the effect of the eddy field on the large-scale, long-time evolution of the tracer is represented as an enhancement

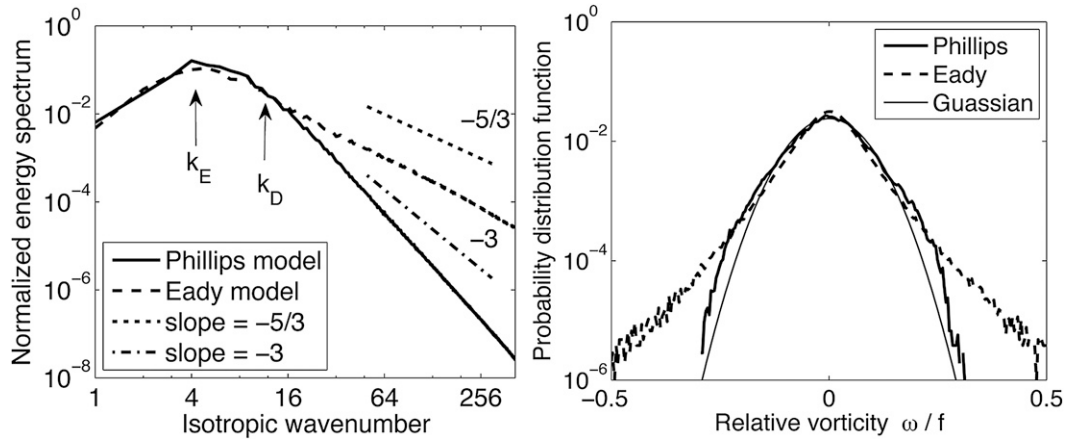


FIG. 1. (left) Equilibrium energy spectra in the Phillips and Eady models. The most energetic eddy wavenumber $k_E = 2\pi/L_E$ and the deformation wavenumber $k_D = 2\pi/L_D$ are indicated (where L_E and L_D are the nondimensional eddy scale and deformation radius, respectively). Also shown are spectral slopes of $k^{-5/3}$ and k^{-3} for comparison. (right) Surface vorticity probability distribution functions for the two models. Also shown is a Gaussian distribution with the same mean and variance as the Eady model flow.

of the molecular diffusivity (Tennekes and Lumley 1972; Majda and Kramer 1999; Vallis 2006).

In the Lagrangian framework, the position $\mathbf{x}_\alpha(t)$ of a particle satisfies the evolution equation

$$\frac{d}{dt}\mathbf{x}_\alpha(t) = \mathbf{u}_\alpha(t), \quad \alpha = \mathbf{x}_\alpha(0), \quad (5)$$

where $\mathbf{u}_\alpha(t) \equiv \mathbf{u}(\mathbf{x}_\alpha, t)$ is the fluid velocity interpolated to particle’s position. For convenience, each particle is labeled by its initial condition. In both model flows, particles were initialized at every grid point in the upper layer (a total of 1024^2 particles per model). A bicubic interpolation scheme was used to calculate the model flow at the particle position, and the particles were advected by solving (5) using a fourth-order Runge–Kutta scheme with a time step matching that of the model (roughly 7 and 3 min for the Phillips and Eady models, respectively). The resulting Lagrangian trajectories can then be analyzed to obtain a statistical description of the dynamics of single particles (absolute diffusivity) and particle pairs (relative diffusivity and finite-time Lyapunov exponents).

Finally, quasi-Lagrangian diagnostics are calculated in a frame that is neither fixed nor comoving with fluid parcels. This is the case for the “effective diascalar diffusivity,” which measures the instantaneous scalar flux across tracer isocontours as measured in a coordinate system chosen to coincide with an advected–dissipated scalar field $C(\mathbf{x}, t)$ (note that this coordinate system is not quite Lagrangian because tracer contours will slip with respect to streamlines owing to the effect of diffusion).

We review the basic properties of each diagnostic below.

a. Absolute diffusivity

The simplest diagnostic of mixing derived from virtual particle trajectories is the absolute diffusivity, which is defined as the rate of change of the absolute dispersion D_{abs} ,

$$K_{\text{abs}}(t) = \frac{1}{2} \frac{d}{dt} D_{\text{abs}}(t), \quad D_{\text{abs}}(t) = \langle |\mathbf{d}_\alpha(t)|^2 \rangle_\alpha, \quad (6)$$

where $\mathbf{d}_\alpha(t) = \mathbf{x}_\alpha(t) - \alpha$ is the absolute displacement of particle α from its initial position and $\langle \cdot \rangle_\alpha$ denotes averaging with respect to particle index. Equation (6) can also be expressed in terms of the Lagrangian velocity autocorrelation function as

$$K_{\text{abs}}(t) = \int_0^t ds \langle \mathbf{u}_\alpha(t) \cdot \mathbf{u}_\alpha(t-s) \rangle_\alpha. \quad (7)$$

Figure 2 shows $K_{\text{abs}}(t)$ for the Phillips and Eady models. On short times, we expect the Lagrangian velocity autocorrelation function to be constant and approximately equal to twice the mean kinetic energy $2E$ so that $K_{\text{abs}} \propto t$, as shown. Thus, particle displacements increase ballistically and $\mathbf{d}_\alpha(t) \approx \mathbf{u}_\alpha(t)t$. On long times, the displacement is expected to grow as a random walk so that $D_{\text{abs}} \propto t$ and K_{abs} is constant.

b. Eddy diffusivity

In the continuum limit, the probability distribution function of particle positions is equivalent to the

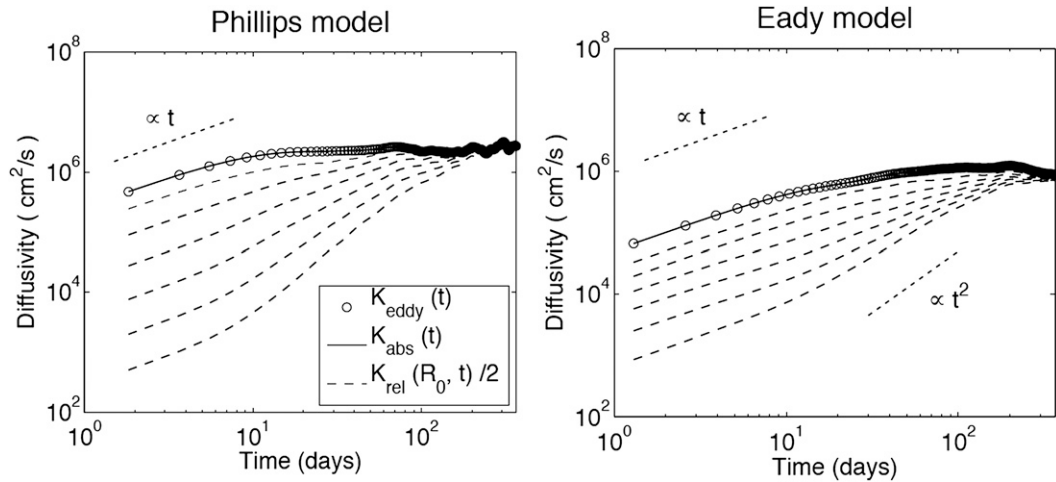


FIG. 2. Log-log plot of the absolute and relative diffusivities and the trace of the eddy diffusivity tensor vs time for the Phillips and Eady models. Relative diffusivities were calculated for initial particle separations of (from bottom to top) $R_0 = 1, 2, 4, 8, 16,$ and 32 km. Dotted lines indicate predicted short time scaling of t and, for the Eady model, the predicted inertial-range scaling of t^2 .

concentration of a passively advected tracer field. Under statistically homogeneous and stationary random stirring, the absolute diffusivity reproduces the familiar eddy diffusivity emerging from mixing length arguments or homogenization theory (Taylor 1921; Majda and Kramer 1999). The eddy diffusivity can be calculated by decomposing the total concentration field into a large-scale mean gradient and a rapidly varying small-scale component,

$$C(\mathbf{x}, t) = \mathbf{G} \cdot \mathbf{x} + c(\mathbf{x}, t). \quad (8)$$

The (source free) tracer evolution equation is then

$$\partial_t c + \mathbf{u} \cdot \nabla c + \mathbf{G} \cdot \mathbf{u} = \kappa \Delta c. \quad (9)$$

Note that the mean gradient term $\mathbf{G} \cdot \mathbf{u}$ in (9) plays the role of the time-varying source–sink in (4). The turbulent flux of scalar c can be expressed in terms of the eddy diffusivity tensor via the usual flux–gradient relation,

$$\langle \mathbf{u}c \rangle = -\mathbf{K}_{\text{eddy}} \mathbf{G}. \quad (10)$$

Figure 2 shows the trace K_{eddy} of the full eddy diffusivity tensor—calculated using two scalar fields with orthogonal mean gradients—superimposed on the absolute diffusivity K_{abs} . For both the Phillips and Eady models, the two diffusivities are essentially indistinguishable. Thus, we conclude that the number of particles used is sufficient to accurately calculate both Eulerian and Lagrangian quantities and does not introduce any additional sources of model error, and we henceforth treat K_{abs} and K_{eddy} as equivalent.

c. Relative diffusion

The relative diffusivity is defined as the rate of change of the relative dispersion D_{rel} ,

$$K_{\text{rel}}(R_0, t) = \frac{1}{2} \frac{d}{dt} D_{\text{rel}}(R_0, t),$$

$$D_{\text{rel}}(R_0, t) = \langle |\mathbf{r}_{\alpha\beta}(t)|^2 \rangle_{|\alpha-\beta|=R_0}, \quad (11)$$

where $\mathbf{r}_{\alpha\beta}(t) = \mathbf{x}_\alpha(t) - \mathbf{x}_\beta(t) = \mathbf{d}_\alpha(t) - \mathbf{d}_\beta(t) + \mathbf{R}_0$ is the relative separation of particles α and β at time t and $\langle \cdot \rangle_{|\alpha-\beta|=R_0}$ denotes averaging with respect to particles initially separated by a distance $R_0 = |\mathbf{R}_0|$. The rate of change of the particle separation is given by

$$\frac{d}{dt} \mathbf{r}_{\alpha\beta}(t) = \mathbf{v}_{\alpha\beta}(t) = \mathbf{u}_\alpha(t) - \mathbf{u}_\beta(t), \quad (12)$$

so that (11) becomes

$$K_{\text{rel}}(R_0, t) = \langle \mathbf{R}_0 \cdot \mathbf{v}_{\alpha\beta}(t) \rangle_{|\alpha-\beta|=R_0}$$

$$+ \int_0^t ds \langle \mathbf{v}_{\alpha\beta}(t) \cdot \mathbf{v}_{\alpha\beta}(t-s) \rangle_{|\alpha-\beta|=R_0} \quad (13)$$

For spatially homogeneous flows, the first term on the right-hand side of (13) vanishes (Babiano et al. 1990). Using (7) and (12), it can then be shown that

$$K_{\text{rel}}(R_0, t) = 2K_{\text{abs}}(t) - 2\Theta(R_0, t), \quad (14)$$

where

$$\Theta(R_0, t) = \int \langle \mathbf{u}_\alpha(t) \cdot \mathbf{u}_\beta(t-s) \rangle_{|\alpha-\beta|=R_0} ds \quad (15)$$

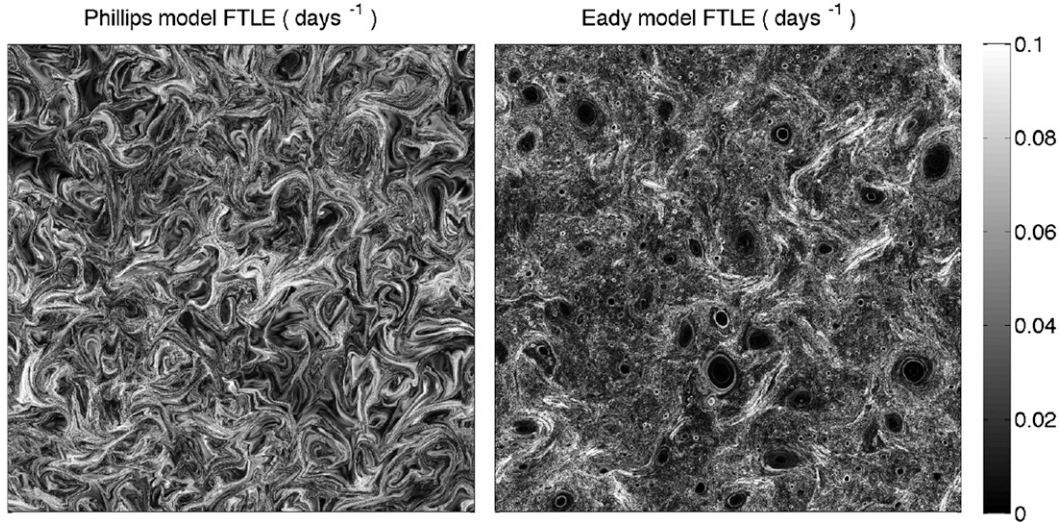


FIG. 3. 1024 km \times 1024 km snapshots of FTLE field for (left) Phillips and (right) Eady models after 64-day integration time.

is the two-particle, two-time Lagrangian velocity autocorrelation function. On sufficiently long time scales, particles that are initially close together will become decorrelated and K_{rel} will be approximately twice the absolute diffusivity, as shown in Fig. 2. The closer the particles are initially separated, the more slowly Θ approaches zero. On short times, the separation velocity $\mathbf{v}_{\alpha\beta}$ is approximately constant so that $K_{\text{rel}} \propto t$ as for the absolute diffusivity. This behavior can also be seen in Fig. 2.

On intermediate time scales, the temporal evolution of the relative diffusivity is dependent on the slope of the kinetic energy spectrum $E(k) \propto k^{-n}$. For sufficiently shallow spectral slopes $1 < n < 3$, the separation velocity is determined by the instantaneous separation of the particles and particle dispersion is spectrally local. Standard scaling arguments (Morel and Larcheveque 1974; Bennett 1984; Babiano et al. 1985) and stochastic flow models (Majda 1993, 1994; Majda and Kramer 1999; Piterbarg 2005) predict an inertial-range scaling of

$$D_{\text{rel}} \propto t^{4/(3-n)}, \quad K_{\text{rel}} \propto t^{(n+1)/(3-n)}, \quad 1 < n < 3. \quad (16)$$

For the Eady model, $n = 5/3$ and (16) reproduces the well-known Richardson scaling law (Richardson 1926),

$$D_{\text{rel}} \propto t^3, \quad K_{\text{rel}} \propto t^2 \quad (\text{Eady model}). \quad (17)$$

For steep spectral slopes $n \geq 3$, the separation velocity is controlled by eddies on the energy-containing scale so that particle dispersion is spectrally nonlocal (Batchelor 1952),

$$D_{\text{rel}} \propto e^{\gamma t}, \quad K_{\text{rel}} \propto e^{\gamma t}, \quad n \geq 3 \quad (\text{Phillips model}). \quad (18)$$

d. Lyapunov exponents

The FTLE is calculated by considering how an infinitesimally small, initially circular patch of tracer centered on the particle α is deformed into an ellipse as it is rotated and stretched by the flow, where the rate of deformation is given by the Jacobian for the local flow $S_{\alpha}^{ij} = \partial_i u_{\alpha}^j$. The FTLE for the particle trajectory indexed by α at time t is given by

$$\lambda_{\alpha}(t) = \ln m_{+}/2t, \quad (19)$$

where $m_{+}(t)$ is the square of the semimajor axis of the elliptical tracer patch (Abraham and Bowen 2002). For each time t , (19) provides a measure of the integrated strain along the trajectory of particle α and can be plotted at the starting point of each particle.

Figure 3 shows 1024 km \times 1024 km snapshots of the finite-time Lyapunov exponent field calculated using particle trajectories integrated for 64 days. These snapshots are remarkably dissimilar. The FTLE field of the Phillips model is characterized by filaments of roughly the same scale, consistent with nonlocal straining at the dominant eddy scale due to a steep submesoscale kinetic energy spectrum. On the other hand, the Eady model exhibits a large number of low-FTLE “voids” on every scale, separated by high-FTLE filaments. These voids are caused by long-lived vortices that trap particles within them leading to very low integrated straining within vortex cores, whereas particles in the inter-eddy

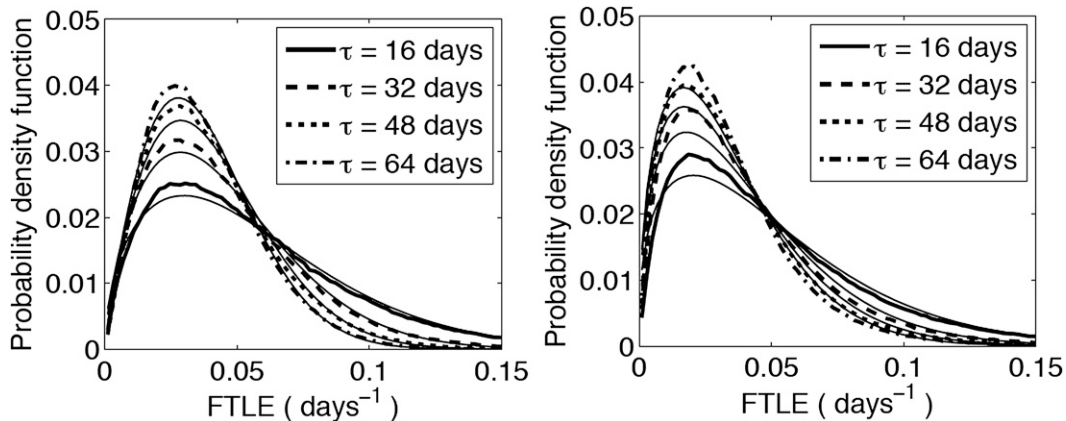


FIG. 4. FTLE distributions for the (left) Phillips and (right) Eady models after 16-, 32-, 48-, and 64-day integration times. Thin lines indicate best-fit Weibull distributions.

regions experience much more straining along their trajectories and so carry much larger FTLE values.

Differences can also be seen in the probability density functions of the FTLEs in the two models, shown in Fig. 4, although they are not as immediately apparent as in the snapshots of the full FTLE field. As is typical of turbulent and chaotic flows, the FTLE distributions depicted in Fig. 4 are initially close to a Rayleigh distribution: indeed, if the components of the straining field were independent Gaussian random variables, then the rms strain and hence the instantaneous FTLE field would have a Rayleigh distribution (Conradsen et al. 1984). As the integration time increases, the PDF becomes more Gaussian and the mean of the distribution decreases. The Gaussianity results from an effective central limit theorem as the tracer experiences a large number of essentially independent, statistically identical strains. The decrease of the mean arises because any choice of infinitesimal circular patch of tracer will not be consistently stretched by the flow along the major axis of the ellipse into which it evolves, so the time-averaged effect of the stretching will fall below the spatially (or ensemble) averaged infinitesimal stretching rates, which is what determines the FTLE at very short times. In the very long time limit, the distribution tends toward a delta function centered on the global Lyapunov exponent for the system.

Recently, Waugh and Abraham (2008) analyzed FTLE distributions derived from virtual particles advected by altimetric velocity fields and found that the PDFs were typically well approximated by a Weibull distribution,

$$P(\lambda) = \frac{b}{a} \left(\frac{\lambda}{a}\right)^{b-1} \exp\left[-\left(\frac{\lambda}{a}\right)^b\right], \quad (20)$$

where a is the scale parameter (determining how stretched out the distribution is and closely related to

the mean of the PDF) and b is the shape parameter, which can take values of 1 (exponential distribution), 2 (Rayleigh distribution), 3.6 (approximately Gaussian), or any value in between (Conradsen et al. 1984). In Fig. 4, the relevant best-fit Weibull distributions are shown by dashed lines. The dependence of the fitted parameters on the integration time is shown in Fig. 5. The ensemble mean of the FTLE distribution {which in the Weibull distribution [(20)] is simply $a\Gamma(1 + b^{-1})$, where Γ is the gamma function} behaves very like the scale parameter a (not shown), asymptotically decaying from a peak at $t = 0$ to a constant value in the ergodic limit as particles randomly sample the entire flow. On finite time, as the FTLE PDF narrows and moves toward smaller mean values, the shape parameter b likewise increases toward the limit 3.6, corresponding to a Gaussian distribution, as seen in Fig. 5. Although the fitted parameters for the two models are very similar, the shape parameter b is systematically smaller in the Eady model than in the Phillips model, corresponding to a more skewed distribution and again reflecting the large population of long-lived vortices with low-FTLE cores.

e. Effective diascalar diffusivity

The effective diascalar diffusivity exploits the fact that, on transforming to a quasi-Lagrangian coordinate system defined by the area $A(C, t)$ enclosed by the tracer isocontour $C^*(\mathbf{x}, t) = C$, the advection diffusion equation [(4)] with $S = 0$ reduces to the following one-dimensional diffusion equation (Nakamura 1996; Shuckburgh and Haynes 2003; Nakamura 2008),

$$\frac{\partial}{\partial t} C = \frac{\partial}{\partial A} \left[D(C, t) \frac{\partial C}{\partial A} \right],$$

$$D(C, t) = \kappa \left(\frac{\partial A}{\partial C} \right)^2 \frac{\partial}{\partial A} \int_{C^* \leq C} dA |\nabla C^*|^2. \quad (21)$$

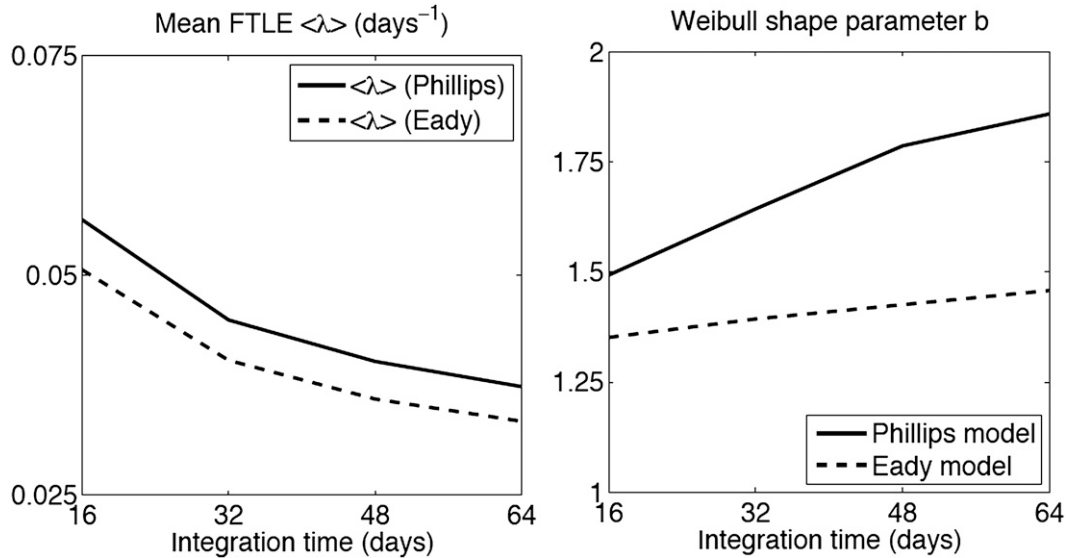


FIG. 5. Properties of FTLE distribution as a function of integration time: (left) mean FTLE λ and (right) Weibull shape parameter b .

Here, $D(C, t)$ is a positive-definite diffusion coefficient measured in area coordinates and therefore has units of (area)²/(time) rather than the usual (length)²/(time). Commonly, $D(C, t)$ is normalized by some characteristic area in the system, such as that of the domain, $A_0 = L_0^2$, to give the instantaneous effective diascalar diffusivity across the tracer isocontour $C^* = C$,

$$K_{\text{eff}}(C, t) = D(C, t)/L_0^2. \quad (22)$$

The effective diascalar diffusivity $K_{\text{eff}}(C, t)$ offers a number of appealing properties as a diagnostic of mixing: it provides a measure of the instantaneous diascalar flux arising from the combined effects of molecular diffusion and the stretching of tracer filaments by the stirring field and thus requires no spatial or temporal averaging to compute; it captures nonconservative, irreversible processes only, filtering out the reversible undulations of the tracer isocontour that contribute nothing to the overall transport; and it is a natural diagnostic for identifying transport barriers and their effect on the global transport properties of the flow (Nakamura 2001; Shuckburgh and Haynes 2003; Nakamura 2008).

To calculate the effective diascalar diffusivity in the Phillips and Eady models, an initially circular patch of tracer concentration with Gaussian cross section is released in the center of the domain (Fig. 6). As time evolves, the tracer isocontours are deformed by the underlying flow (Fig. 7) and dissipated on small scales via a Laplacian diffusion term $\kappa \nabla^2 C$ with numerical diffusivity $\kappa = 1 \times 10^{-5} \text{ cm}^2 \text{ s}^{-1}$ for the Phillips flow and

$\kappa = 2 \times 10^{-7} \text{ cm}^2 \text{ s}^{-1}$ for the Eady flow. These values were chosen such that (i) they are large enough to ensure numerical stability of the tracer advection scheme and (ii) they are small enough that the effective diascalar diffusivity is essentially independent of the precise value of the numerical diffusivity in mixing regions (Shuckburgh and Haynes 2003). Thus, even though the numerical diffusivities differ by two orders of magnitude, it is still meaningful to compare effective diascalar diffusivities in the two models because they are not dependent on the subgrid-scale diffusion.

Again, strong differences in the nature of the stirring are visible in the tracer snapshots, with the Phillips flow (Fig. 7, left) dominated by large-scale eddies and the Eady flow (Fig. 7, middle) exhibiting stirring of the tracer isocontours on all scales. For each instantaneous snapshot of the tracer field $C_i(\mathbf{x}) = C(\mathbf{x})$, the area $A(C)$ enclosing values of tracer concentration equal to or less than C is a monotonically increasing function of C with values between $A(C_{\text{min}}) = 0$ and $A(C_{\text{max}}) = A_0$. Thus, given $C(\mathbf{x}, t)$, it is straightforward to calculate $|\nabla C|$, $A(C, t)$, and $\partial A/\partial C$ at each instant and hence to calculate $K_{\text{eff}}(C, t)$ for each tracer isocontour using (21) and (22). The results of this calculation are shown in Fig. 7 (right). In both flows, the strongest mixing (characterized by the largest values of the effective diascalar diffusivity) tends to occur where the diascalar gradient is steepest and the tracer contours are closely spaced. As time evolves, there is an initial adjustment phase of several eddy turnover times as the tracer isocontours align with the flow and K_{eff} increases with time (Fig. 8). On very

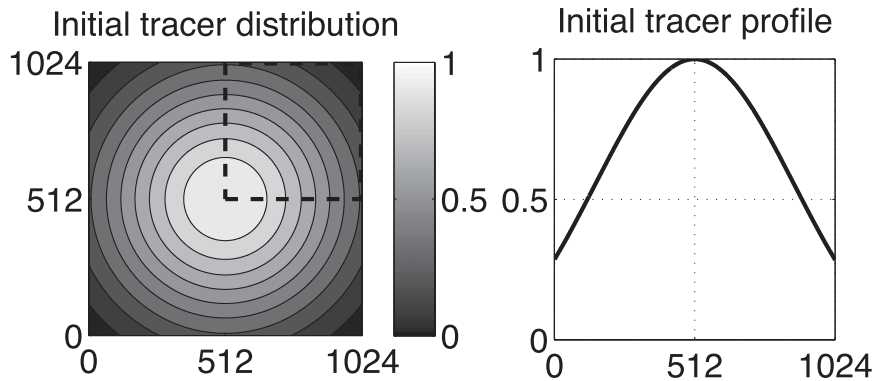


FIG. 6. Initial tracer (left) distribution and (right) profile used to calculate the effective diascalar diffusivity K_{eff} . The dashed box indicates the region of the domain depicted in Fig. 7.

long times, the tracer field must ultimately decay to zero in the absence of a source. For the purposes of this study, we focus our attention on the initial adjustment phase (up to 64 days, roughly four turnover times) as we did with the relative dispersion of particle pairs.

4. Resolution dependence of mixing diagnostics in quasigeostrophic turbulence

The mixing and stirring diagnostics discussed in the preceding section were measured using tracers advected with velocity fields available at every grid point (a spatial resolution of $\Delta x = 2$ km) and every model time step (temporal resolutions of $\Delta t = 7$ min for the Phillips model and 3 min for the Eady model). These diagnostics constitute a truth signal against which we now compare the same diagnostics obtained from velocity fields subsampled in space and time. To quantify the model error arising from spatial and temporal subsampling, we calculate the normalized error of a given mixing diagnostic *viz.*,

normalized error

$$= 1 - \frac{\text{diagnostic measured with subsampled flow}}{\text{diagnostic measured with true flow}}. \quad (23)$$

a. Spatial resolution dependence

Spatial subsampling of the flow was achieved by truncating the Fourier spectrum of the streamfunction ψ at high wavenumbers $|\mathbf{k}| \geq k_{\text{cut}}$, effectively filtering out features of the velocity field on scales smaller than $\Delta x = 2\pi/k_{\text{cut}}$. In this way, velocity fields with spatial resolutions of $\Delta x = 8, 16, 32, 64,$ and 128 km were obtained and used to advect tracers every model time step (recall that the deformation radius for both models is approximately

85.3 km). Note that Fourier truncation is not the same as subsampling spatial grid points, because in the latter case high-wavenumber fluctuations will be aliased into the low-wavenumber band. Fourier truncation throws away these aliased fluctuations, resulting in a decrease in the total energy of the observed flow. On the other hand, Fourier truncation leaves unchanged the lowest wavenumbers, whose temporal evolution remains dynamically consistent with the fully resolved simulation. In this way, we are able to directly compare tracer mixing in the fully resolved flow with mixing due to large scales alone. The role of spatial subsampling and aliasing on altimetric velocity fields is explored in a companion article (S. R. Keating et al. 2010, unpublished manuscript).

Figure 9 shows the normalized error versus sampling resolution Δx for the suite of diagnostics considered. In both the Phillips and Eady models, we find that the absolute diffusivity is fairly insensitive to the spatial resolution of the advecting velocity field, a result that is consistent with the intuition that absolute diffusion is controlled by the slowly evolving large-scale modes (Taylor 1921; Davis 1982), which are likely to be captured even at very poor spatial resolution.

In contrast, the Phillips and Eady models display very different behavior for the relative diffusivity (calculated at $t = 16, 32, 48,$ and 64 days, with an initial separation of $R_0 = 1$ km). In the Phillips model, the normalized error remains fairly small for all spatial resolutions Δx up to roughly the deformation scale. That is, two-particle dispersion in the Phillips model is found to be quite insensitive to truncation of the local scales of motion, consistent with the paradigm of spectrally nonlocal dispersion in which particle dispersion is controlled by the low-wavenumber energy-containing scales. Above the deformation radius, a sharp increase in the normalized error is observed that can be accounted for by a transition from a steep k^{-3} kinetic energy spectrum in the

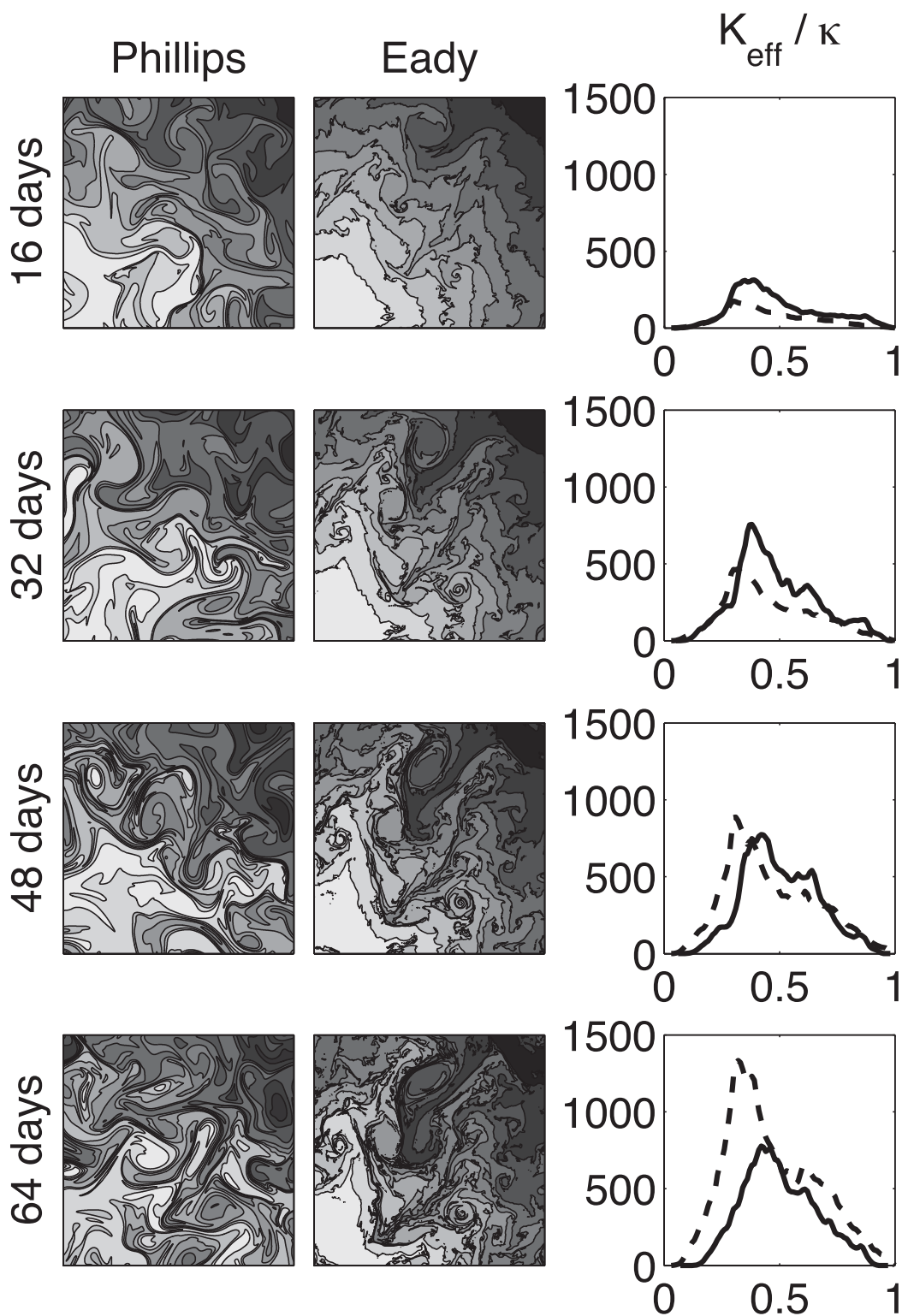


FIG. 7. Snapshots of tracer concentration in the Phillips and Eady model at 16, 32, 48, and 64 days after the initial tracer release. The region shown corresponds to the northeast quadrant of the full domain, indicated by the dashed box in Fig. 6. The color map in each figure is the same as that used in Fig. 6. (right) The effective diatomic diffusivity K_{eff} , normalized by the molecular diffusivity κ at each snapshot time as a function of tracer concentration for the Phillips (solid line) and Eady (dashed line) models.

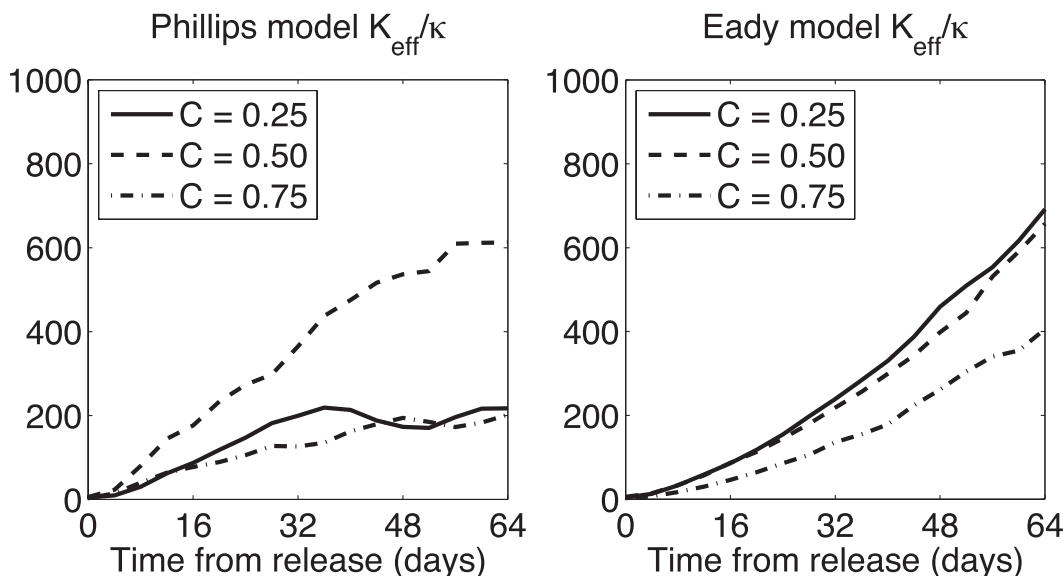


FIG. 8. Time evolution of the effective diascalar diffusivity K_{eff} , normalized by the numerical diffusivity κ , for the Phillips and Eady models. The values of K_{eff}/κ shown correspond to the tracer isocontours $C = 0.25, 0.5,$ and 0.75 .

forward cascade range to a shallow $k^{-5/3}$ spectrum in the inverse cascade, with an associated switch from nonlocal to local dispersion and an increase in the sensitivity to the filtered scales. These same qualitative features are seen for the relative diffusivity in the Phillips model at $t = 16, 32, 48,$ and 64 days from release. As time increases, the normalized error decreases as the particle pair becomes decorrelated and the relative diffusivity, like the absolute diffusivity, becomes more and more controlled by the large-scale slow modes.

In the Eady model, the normalized error for the relative diffusivity is considerably larger than that of the Phillips model at every sampling resolution. Moreover, the error increases steadily as Δx increases, with no sudden jump in error at the deformation scale, as in the Phillips model. Again, this is consistent with the picture of local dispersion in which the relative diffusivity is controlled by turbulent eddies on the scale of the particle pair separation and hence is highly sensitive to truncations of the kinetic energy spectrum that do not resolve these scales. Likewise, the normalized error decreases with increasing time as the pair separation grows toward larger (resolved) scales and the relative diffusivity asymptotes toward twice the value of the absolute diffusivity.

Qualitatively very similar results are seen for the effective diascalar diffusivity K_{eff} across the $C = 0.5C_{\text{max}}$ tracer concentration isocontour and the mean of the FTLE distribution $\bar{\lambda}$ (each shown for $t = 16, 32, 48,$ and 64 days). In the Phillips model, these diagnostics are found to be weakly sensitive to the spatial sampling resolution up to roughly the deformation radius, where

a sudden increase in the normalized error is observed, consistent with a transition from nonlocal dispersion on small scales to local dispersion on large scales. The normalized errors are noticeably larger in the Eady model and again increase steadily as the spatial resolution is coarsened, with no sharp jump at the deformation radius observed. Once again, this is consistent with the paradigm of spectrally local dispersion in both the forward and inverse cascade ranges.

To characterize their sensitivity to the spatial resolution, the FTLE distributions obtained from the particle trajectories and straining fields calculated using the subsampled velocity fields were fitted with a Weibull distribution. The normalized error for the Weibull scale parameter a (not shown) was found to have a very similar behavior as that of the mean FTLE $\langle \lambda \rangle$, as could be expected from the close relationship between these quantities: namely, $\langle \lambda \rangle = a\Gamma(1 + b^{-1})$, where Γ is the gamma function. In contrast, the Weibull shape parameter b shows little variation with spatial resolution for both the Phillips and Eady models, although the Eady model shows a more consistent decrease in this parameter as the spatial resolution is coarsened.

b. Temporal resolution dependence

The flow was temporally subsampled by using snapshots of the flow taken every $\Delta t = 1, 2, 4, 8,$ or 16 days (recall that the eddy turnover time for both models is approximately 15 days). Typically, altimetry-derived velocity snapshots are linearly interpolated in time to form velocity time series with a higher frequency; for instance,

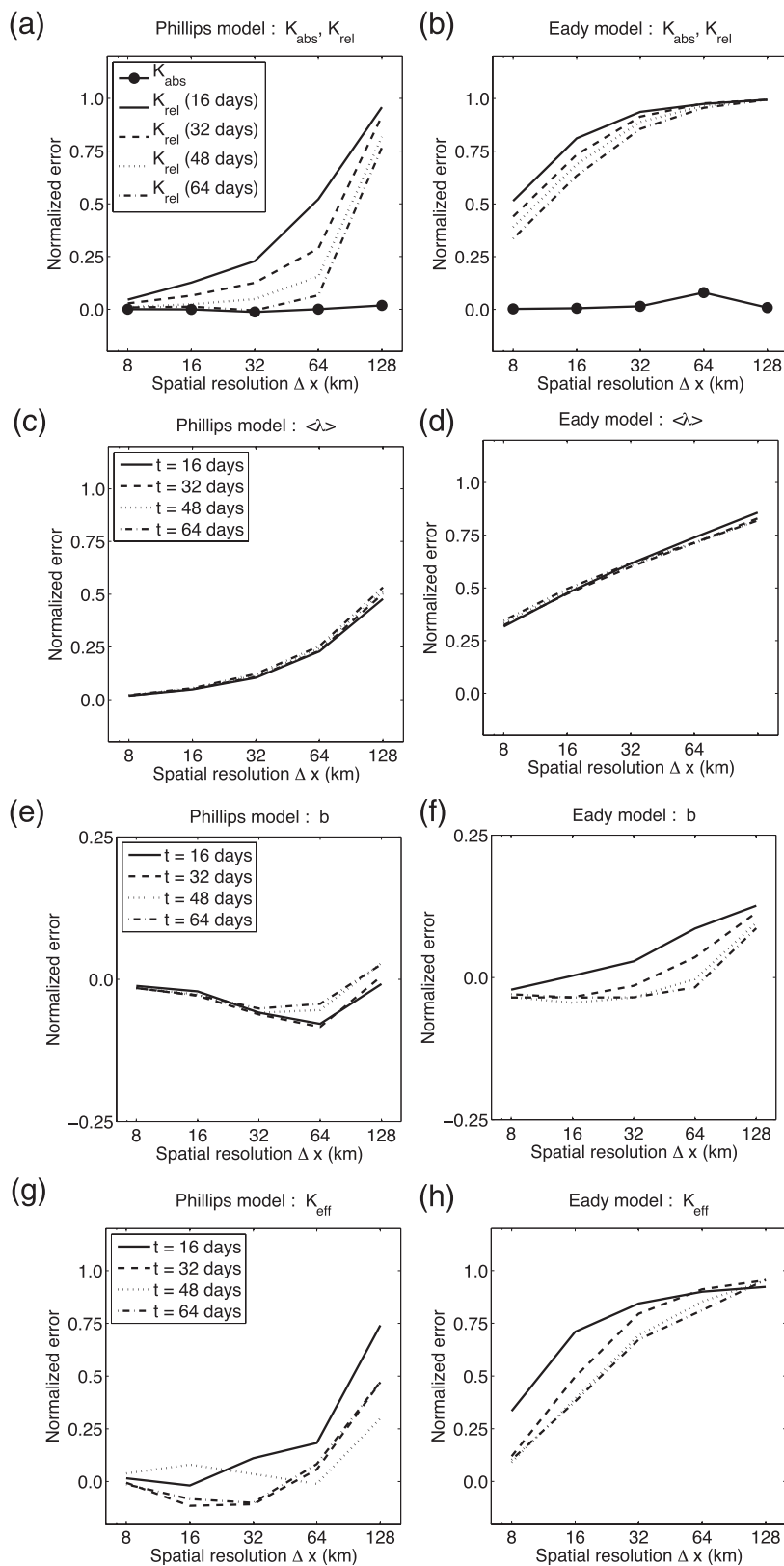


FIG. 9. Normalized error vs spatial sampling resolution Δx for mixing diagnostics in the (left) Phillips and (right) Eady models.

two successive snapshots of the flow separated in time by 8 days will be linearly interpolated to form 9 different daily snapshots (days 0 through 8), which are then used to advect the tracers once per day. However, this method potentially introduces a new source of error arising from the fact that the linearly interpolated snapshots will not in general be solutions to any given nonlinear equation of motion.

To elucidate these possibly competing sources of model error arising from temporal subsampling and linear interpolation in time we considered two subsampling strategies, respectively:

- 1) Tracers are advected with snapshots of the velocity field taken every Δt days: that is, only the observed flow is used to advect tracers, without any interpolation.
- 2) Tracers are advected every model time step (as in the truth signal) by linearly interpolating between successive observations of the velocity field to form snapshots every 7 (for the Phillips model) or 3 min (for the Eady model).

In this way, we can examine the effect of temporal subsampling alone and then compare these results with those obtained by interpolating the velocity field to the same frequency as the truth signal.

For both of the temporal subsampling schemes considered, we found strong numerical instability in the pseudospectral time stepper used to advect the scalar fields. This is unsurprising given the extremely long time steps (up to 16 days) used to advect the fields with velocity fields with strong small-scale gradients.

The results for sampling strategy 1 (no interpolation in time) for particle-based diagnostics are shown in Fig. 10. As in the case of spatial subsampling, the absolute diffusivity is found to be the least sensitive to the sampling resolution of the diagnostics considered, although somewhat more sensitivity is seen in the Phillips model than in the Eady model. For the remaining particle-based diagnostics, it is difficult to discern any strong distinction between the two models in the behavior of the normalized error versus temporal resolution. The relative diffusivity shows, for both models, a general increase in the normalized error as Δt is lengthened, but the behavior is nonmonotonic and in some cases there appears to be an improvement in the error for poorer temporal resolutions. Likewise, the normalized error for the fitted Weibull shape parameter displays a nonmonotonic behavior in its temporal resolution dependence, alternately increasing and decreasing with Δt , although the range of variation is not as strong as that of the relative diffusivity. The mean of the FTLE distribution (as well as the fitted Weibull scale parameter; not shown) shows a clearer trend in the temporal resolution dependence of the

normalized error; in this case, the mean is found to increase with respect to the truth signal, precisely the opposite tendency than was observed for the spatial resolution dependence and apparently independent of the spectral locality of the underlying turbulent flow.

We speculate that this complex dependence on the temporal sampling resolution is a consequence of the fact that such a long time step (up to 16 days) is used to advect particles in a highly resolved turbulent flow. In particular, it is expected that particles will “overshoot” or deviate from their true trajectories, resulting in a “scrambling” or randomization of the derived Lagrangian diagnostics. This effect is strongly suggested by Fig. 11, which shows $256 \text{ km} \times 256 \text{ km}$ snapshots of the 64-day FTLE field derived from particle trajectories in the Eady model with $\Delta x = 2 \text{ km}$ and $\Delta t = 3 \text{ min}$ (the truth signal), $\Delta x = 128 \text{ km}$ and $\Delta t = 3 \text{ min}$ (worst spatial resolution), $\Delta x = 2 \text{ km}$ and $\Delta t = 16 \text{ days}$ (worst temporal resolution and no interpolation), and $\Delta x = 2 \text{ km}$, $\Delta t = 16 \text{ days}$ (worst temporal resolution, maximum interpolation), respectively. Each of these figures depicts the same region of the flow, corresponding to the bottom-left corner of the FTLE field shown in Fig. 3.

The FTLE field derived from the truth signal again clearly indicates a number of long-lived coherent structures (vortices) as low-FTLE regions where particles are trapped for long periods and high-FTLE inter-eddy straining regions. Unsurprisingly, this finescale structure is entirely lost as the spatial resolution is coarsened (worst spatial resolution). In addition, the magnitude of the FTLE field decreases significantly as small-scale straining regions are filtered out. The FTLE field calculated using this coarse spatial resolution is essentially independent of the temporal resolution used, with little difference seen as Δt is varied between 3 min and 16 days, a range of almost four orders of magnitude.

On the other hand, the FTLE field derived from poor temporal resolution velocity fields without interpolation has similar magnitudes to that of the truth signal but little of the spatial structure, except on the largest scales. This can be understood as a consequence of the fact that, when Δt for these observations is so long that the distance traveled by a particle in one time step is much longer than the correlation length of the underlying flow, the particle experiences what is basically a random straining field and the measured FTLE value is an integrated version of this scrambled field. Thus, the resulting FTLE field is a patchwork of scrambled “chaotic” regions where Δt is too long to resolve rapid changes in the flow and more quiescent, less noisy regions associated with long-lived eddies, which are better resolved by the velocity field. In section 5, we will build on this simple intuition and construct a rudimentary Courant–Friedrichs–Lewy style

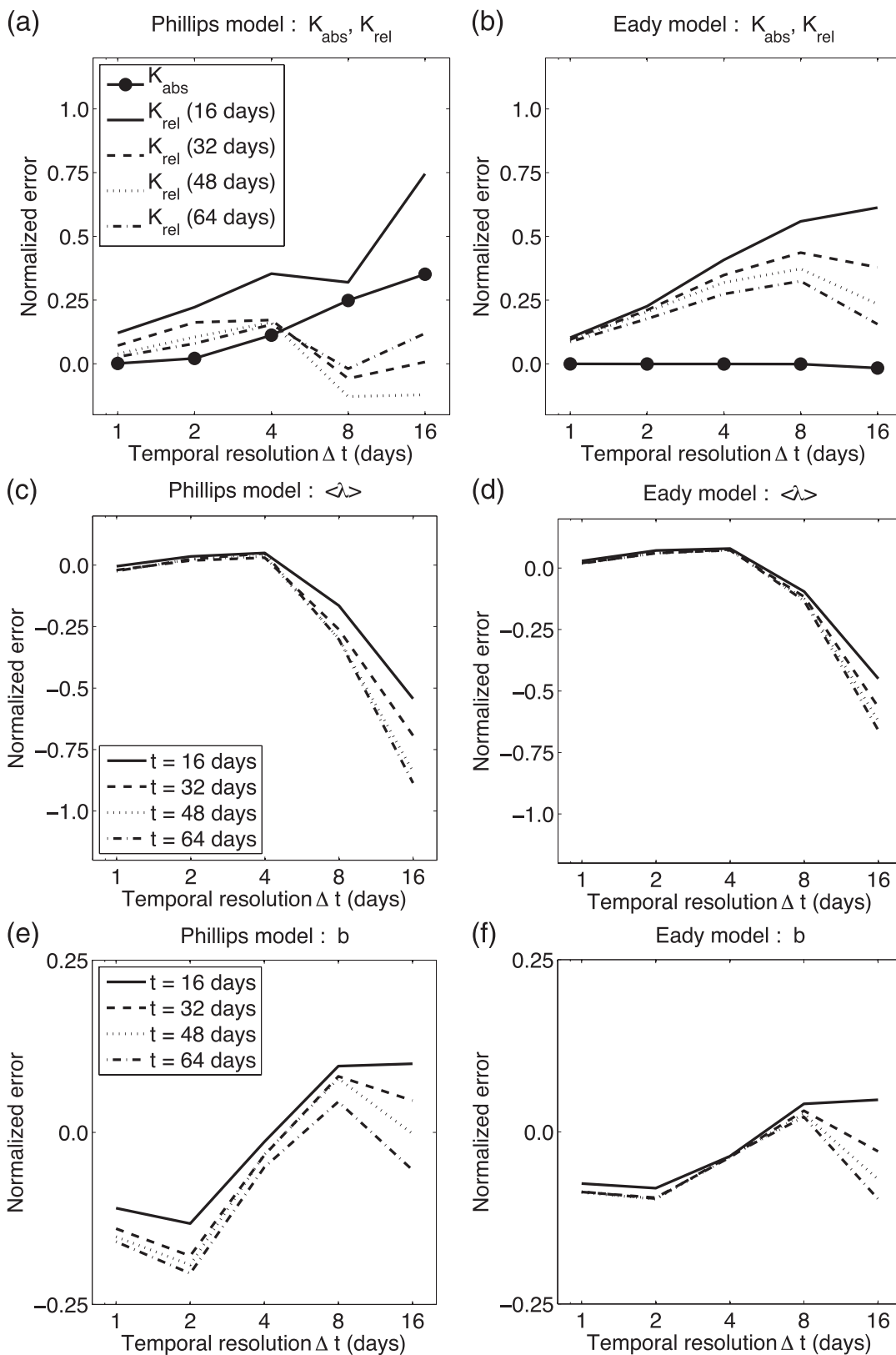


FIG. 10. Normalized error vs temporal sampling resolution Δt for mixing diagnostics in the (left) Phillips and (right) Eady models with no interpolation in time.

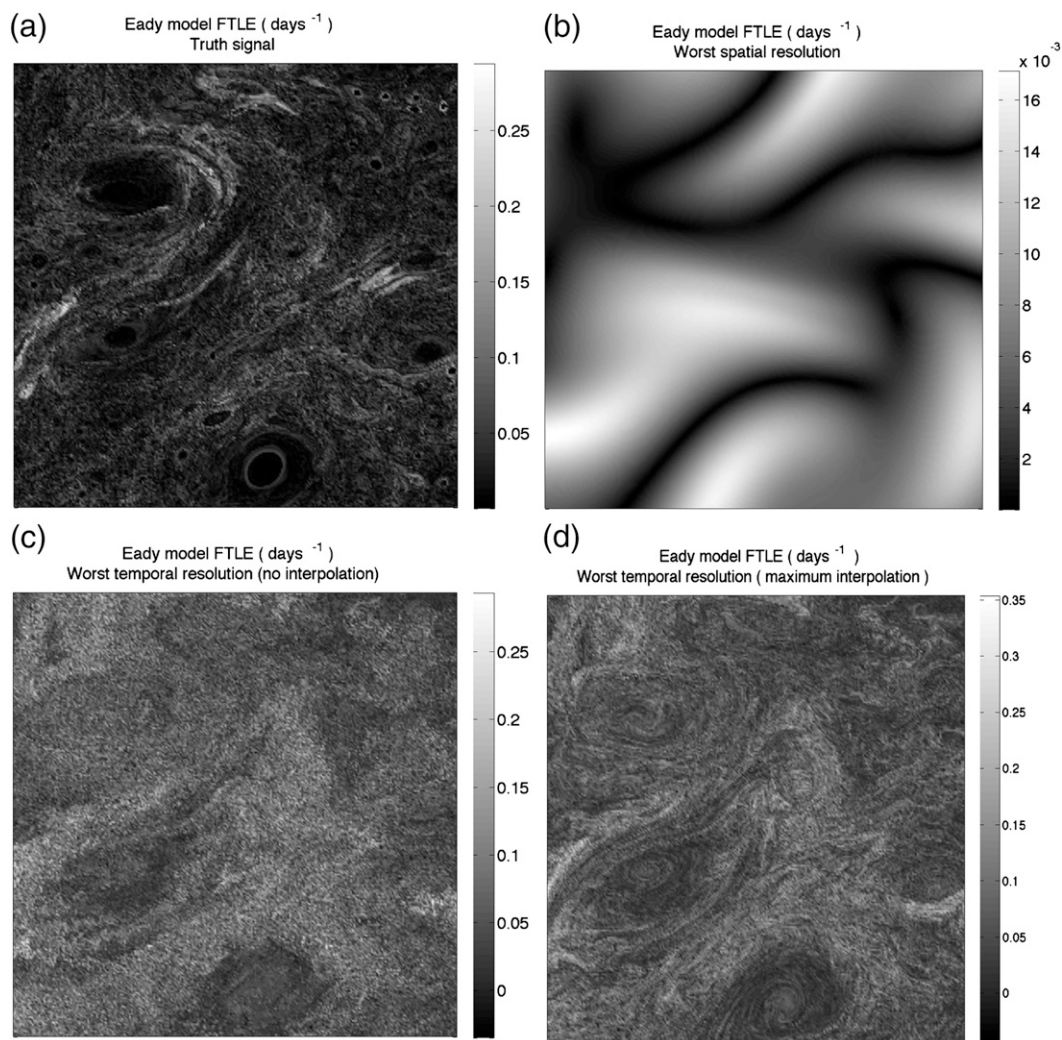


FIG. 11. Snapshots of the 64-day FTLE field derived from the Eady model flow with (top) full resolution (truth signal) and worst spatial resolution and (bottom) worst temporal resolution without and with linear interpolation in time.

criterion for particle overshoot, which will then be used to synthesize the spatial and temporal resolution dependencies of virtual particle-based diagnostics.

The role of particle overshoot on dispersion can be illustrated using the so-called Lyapunov exponents of the second kind (Boffetta et al. 2000; Iudicone et al. 2002). This diagnostic quantifies the predictability of Lagrangian trajectories by measuring the rate of separation of a particle pair in which one member is advected by the true flow and the other is advected by an approximation (or subsample) of that flow,

$$\lambda_{II}(t) = \log \frac{\langle |\mathbf{r}_{\alpha\beta}(t)| \rangle}{R_0}, \quad (24)$$

where $\mathbf{r}_{\alpha\beta}(t)$ is the separation between two particles initially separated by a distance R_0 . Note that (24) is a slightly

different formulation of the FTLE described in section 3, because here we are comparing true and approximate particle trajectories rather than the deformation of an infinitesimal circular patch of tracer comoving with a particle.

Figure 12 shows $\lambda_{II}(t)$ for the Eady model with one particle advected by the true flow and one advected using 16-day snapshots of the flow with no interpolation in time. For comparison, we also plot the FTLEs of the first kind $\lambda_I(t)$ (with both particles advected by the true flow). In all cases, the particle pairs are released at every grid point and initially separated by 1 km with half aligned along the east–west axis and half along the north–south axis. As can be seen, the 16-day snapshots produce more rapid separation of true and approximate trajectories than is the case when both particles are

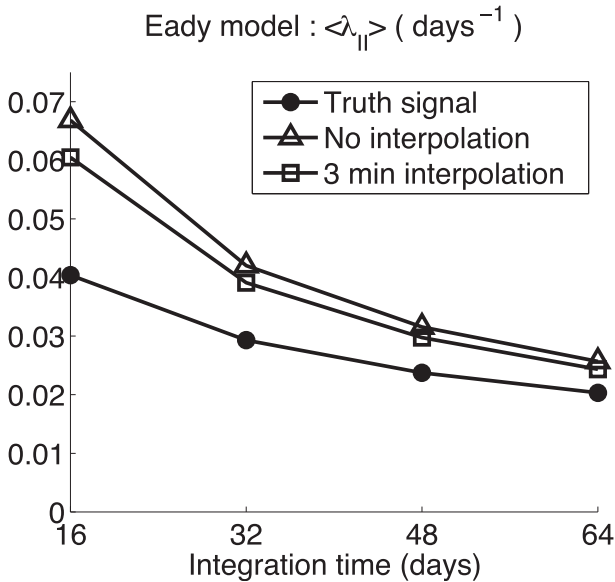


FIG. 12. FTLEs of the second kind vs integration time for particle pairs in which one particle is advected by the true flow and one particle is advected using 16-day snapshots of the flow with no temporal interpolation (triangles) and with linear interpolation to the model time step (squares). Also shown for comparison is the FTLE of the first kind in which both particles are advected with the true flow (filled circles).

advected by the true flow, indicating a loss of Lagrangian predictability due to temporal subsampling.

A natural strategy for ameliorating the effect of particle overshoot is to artificially shorten the advection time step Δt by linearly interpolating between successive observations of the velocity field to form snapshots of a higher frequency. To demonstrate the effects of temporal interpolation, Fig. 12 also shows $\lambda_{II}(t)$ for particle pairs in which the approximate particle trajectory is calculated with 16-day snapshots linearly interpolated to the model time step (3 min). Although the separation of true and approximate trajectories is again much stronger than when both particles are advected by the true flow, temporal interpolation does indeed reduce the rate of separation and improve predictability.

As we have discussed, temporal interpolation potentially introduces a new source of model error due to the lack of a superposition property for nonlinear flows. This model error will be in addition to the underlying error due to temporal underresolution but replaces the error due to particle overshoot. To quantify the error we repeat the analysis carried out for flows that were spatially subsampled and temporally subsampled (without interpolation), now interpolating the velocity field observations so that particles are advected every model time step.

The normalized errors for the particle-based diagnostics are shown in Fig. 13. Once again, the absolute

diffusivity is found to be highly insensitive to the temporal sampling resolution. The relative diffusivities show a monotonic increase in the normalized error with Δt and an improvement over the case with no interpolation in time. The relative diffusivity in the Eady model tends to have higher normalized error than in the Phillips model, although there is no strong difference in the sensitivity of the error to the temporal sampling resolution (i.e., the rate of increase with Δt) in the two models. This would seem to suggest that there is no simple analog of the local/nonlocal dispersion paradigm that was used to explain the observed spatial resolution sensitivity of derived mixing diagnostics. The normalized errors for the mean FTLE, fitted Weibull scale parameter (not shown), and shape parameter are very similar to those found in the case with no temporal interpolation. We suspect this is because particle overshoot effectively scrambles the spatial distribution of the FTLEs but leaves its mean and PDF unchanged. This insensitivity to Lagrangian scrambling suggests that FTLE statistics are likely to be more robust measures of mixing than the spatial distribution of Lyapunov exponents, because they will average out the effects of particle scrambling. Thus, temporal interpolation has little effect on the FTLE statistics, whereas interpolation reproduces more of the fine spatial structure of the FTLE field, even when the temporal resolution is as poor as $\Delta t = 16$ days, as can be seen in Fig. 11.

5. Discussion

We saw in the previous section that using a long time step to advect particles in velocity fields with finescale structure led to significant overshooting of particle trajectories because the distance traveled by the particle during one time step is longer than the correlation length scale of the underlying flow (particularly the spatial gradients of the velocity field). In this situation, the particles experience what is effectively a random straining field and the resulting Lagrangian mixing diagnostics represent a scrambled version of the truth signal. We can make a prediction for the onset of overshoot by constructing a simple Courant–Friedrichs–Lewy style criterion (see, e.g., Durran 1999): namely,

$$\frac{\Delta x}{\Delta t} \ll v_{\max}(\Delta x), \tag{25}$$

where Δx and Δt are the spatial and temporal resolutions and v_{\max} is the maximum observed velocity (in principle a function of the scale Δx). When the maximum distance a particle can travel in a single time step $v_{\max}\Delta t$ is much greater than Δx , the particle will overshoot features of this size or smaller (or rather features with correlation

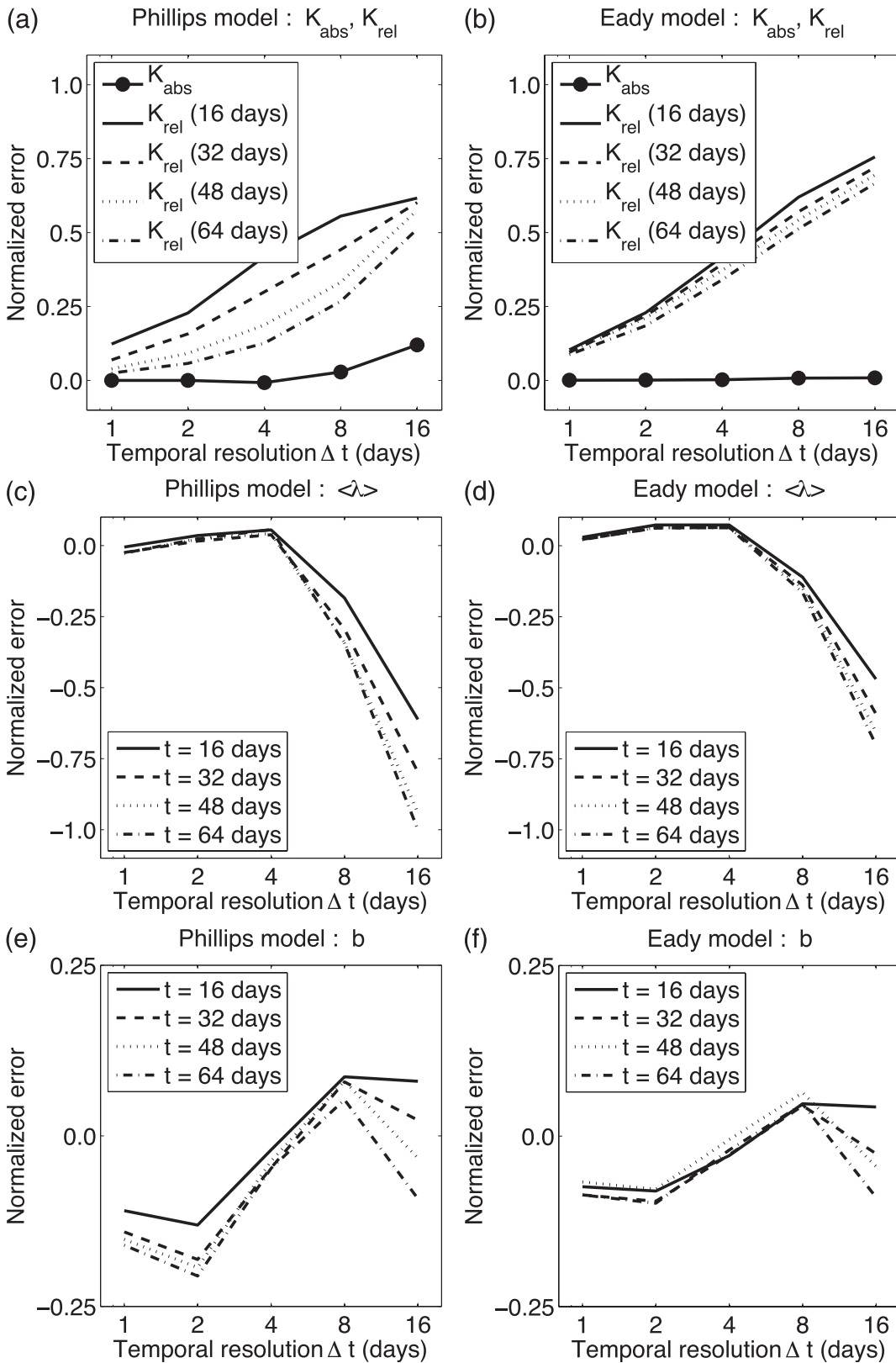


FIG. 13. Normalized error vs temporal sampling resolution Δt for mixing diagnostics in the (left) Phillips and (right) Eady models, with velocity fields interpolated to every model time step.

length scales of the size or smaller). Thus, a particle traveling a distance $v_{\max}\Delta t \gg \Delta x$ in a single time step will escape vortices of radius on the order of Δx , leading to significantly less particle trapping within vortices and spuriously high dispersion as shown in Fig. 12.

The relevant overshoot criterion for the Phillips and Eady models is depicted graphically in Fig. 14. The maximum magnitude for the velocity field v_{\max} was measured for each flow at each spatial resolution and plotted against the corresponding threshold temporal resolution $\Delta t_{\text{crit}} = \Delta x/v_{\max(\Delta x)}$. For values of $\Delta t \gg \Delta t_{\text{crit}}$, the time step is too long to accurately advect particles in the observed velocity field and overshoot becomes an increasingly significant source of model error. As can be seen, v_{\max} was found to have a fairly weak dependence on Δx and the overshoot criterion is well approximated by a linear function of Δx (solid lines shown in Fig. 14). Note that the maximum velocity (typically a few times the rms velocity in each flow) is about 40 cm s^{-1} for the Phillips model, somewhat larger than that for the Eady model, about 12 cm s^{-1} , but both are in the ballpark for typical eddying currents. However, both are smaller than the largest measured velocities obtained from drifters in the real ocean (on the order of meters per second in, e.g., the Gulf Stream). Thus it is likely that, in strongly eddying regions of the ocean, the overshoot criterion might be even more restrictive than shown here.

A crucial feature of Fig. 14 and the overshoot criterion [(25)] is that it is the spatial sampling resolution that sets the threshold value required of the temporal sampling resolution to avoid model error due to particle overshoot. More precisely, it is the length scale of the smallest relevant structures that determines the particle overshoot criterion, and typically the available spatial resolution is not sufficient to fully resolve the flow, so the relevant length scale from the dataset is indeed the spatial resolution. Therefore, the spatial and temporal resolutions are not independent but rather are coupled in the sense that if Δt is larger than the critical value dictated by Δx then particle-based diagnostics will be, to a greater or lesser degree, scrambled, whereas if Δt falls below the threshold the excess temporal resolution does not provide any added value and constitutes an inefficient use of resources, at least in the context of the virtual particle-based diagnostics of interest here.

Also shown in Fig. 14 are spatiotemporal resolutions of two operational altimetry datasets: the first is the widely used AVISO product, which merges data from multiple altimeters and publishes the gridded geostrophic streamfunction and currents; the second is the anticipated SWOT mission, which represents the next generation of satellite-mounted altimeters with significantly higher spatial resolutions. The relevant values for Δx and Δt

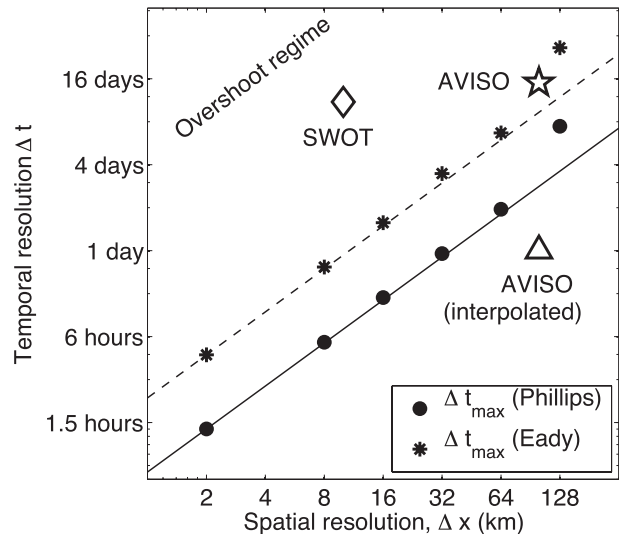


FIG. 14. Threshold temporal resolution for particle overshoot $\Delta t_{\text{crit}} = \Delta x/v_{\max(\Delta x)}$. Solid and dashed lines correspond to the threshold temporal resolution calculated using v_{rms} rather than v_{\max} for the Phillips and Eady model, respectively. Also shown are approximate spatial and temporal resolutions for the SWOT and AVISO products.

correspond approximately to best spatial and temporal correlation scales of the altimetry mapping procedure used by AVISO (Ducet et al. 2000) and the minimum science requirements proposed for SWOT (see <http://swot.jpl.nasa.gov/science>). As can be seen, both of these datasets, particularly the SWOT mission, lie in the overshoot regime, suggesting that using the raw datasets to advect particles could lead to model error that will degrade the accuracy of inferred Lagrangian mixing diagnostics, particularly in regions of high eddy kinetic energy.

As we have discussed, an appealing strategy for ameliorating the impact of overshoot on virtual particle-based diagnostics is to artificially decrease Δt by linearly interpolating the observed velocity fields in time. This approach is widely used in the oceanographic literature where, for example, AVISO velocity datasets available every 7 days are linearly interpolated to form daily snapshots of the upper ocean geostrophic flow field. As pointed out earlier, this strategy also gives rise to additional model error arising from using an unphysical velocity field to advect particles and fields. However, this error is small when compared with the underlying error due to temporal subsampling and is typically justified by a compensatory increase in Lagrangian predictability. The overshoot criterion (25) provides a quantitative estimate of how much temporal interpolation is required to make use of AVISO or SWOT data for offline mixing studies.

It is important to bear in mind that both approaches—advection with and without temporal interpolation—necessarily refer to an artificial velocity field that is piecewise constant in time. Temporal interpolation reduces the time intervals over which the velocity field is treated as artificially steady but could introduce other artifacts resulting from a linear interpolation strategy for a nonlinearly evolving flow. If the interpolation is performed sufficiently finely in time to meet the criterion [(25)] for avoiding particle overshoot, then at least the computed tracer statistics are accurately representing the tracer dynamics in this artificial velocity field. Otherwise, not only is the effective velocity field artificial but the tracer statistics are not even being computed consistently for any specifiable velocity field.

A more sophisticated approach to working with limited spatial and temporal resolution is to attempt to augment the observed data with a model for the unresolved scales. Such schemes, which run the gamut from the family of Lagrangian stochastic models (e.g., Griffa 1996; Berloff and McWilliams 2002; Berloff et al. 2002; Berloff and McWilliams 2003) to fully data-assimilating regional ocean models such as the Massachusetts Institute of Technology general circulation model (MITgcm; Marshall et al. 1997a,b), of course substitute one kind of model error (particle overshoot) for another (a subgrid-scale parameterization for the unresolved scales). However, it is hoped that these new sources of model error can be limited or at least judiciously chosen so that an accurate reconstruction of the mixing and stirring properties of observed velocity fields can be inferred (for an in-depth discussion of some of these issues, see Majda et al. 2010). We will address some of these issues in a companion article (S. R. Keating et al. 2010, unpublished manuscript).

6. Conclusions

In this study, we have sought to elucidate the overlapping effects of spatial and temporal resolution of velocity fields on diagnostics of mixing and stirring derived from virtual tracer particles and fields. We have examined a suite of widely used Eulerian, Lagrangian, and quasi-Lagrangian diagnostics in a pair of closely related but contrasting models of quasigeostrophic turbulence: the Phillips model, which exhibits a steep k^{-3} submesoscale kinetic energy spectrum and in which particle dispersion is strongly controlled by the large-scale modes, and the Eady model, which has a shallow $k^{-5/3}$ spectrum and in which dispersion is governed by the local scales of motion. Although these models are highly idealized, they constitute a valuable best- and worst-case comparison incorporating many of the dynamical features in play in the real ocean: eddies generated by

baroclinic instability, interior or surface-trapped modes, a quiescent or energized submesoscale, nonlocal or local spectral dynamics, and the presence or absence of long-lived submesoscale coherent vortices.

Virtual tracer diagnostics were calculated in both models at full resolution and compared with the same quantities calculated from particles and fields advected by spatial and temporal subsamples of the truth signal. The discrepancy between these two measurements quantifies the model error arising from spatiotemporal subsampling. Tracer diagnostics in the Phillips model are found to be generally insensitive to spatial smoothing of the stirring field, as long as the deformation scale is resolved. Tracer mixing in the Eady model, which exhibits an energized submesoscale spectrum, shows much stronger dependence on the spatial resolution scale, as do tracer diagnostics in the Phillips model with an unresolved deformation scale. This behavior is consistent with the paradigm of local and nonlocal spectral dynamics and reproduces similar findings by Bartello (2000) and Shepherd et al. (2000) in the context of atmospheric mesoscale mixing and Beron-Vera et al. (2008), Rossi et al. (2008), Shuckburgh et al. (2009a), and Poje et al. (2010) in regional ocean studies.

We also systematically studied the temporal dependence of diagnostics, which is of particular interest for mixing studies using altimetric maps because both spatial and temporal resolution are constrained by the satellite orbit. In contrast, previous studies of mixing in ocean models have typically focused on spatial resolution dependence alone, because of the larger computational investment. We find that the temporal sampling error has a complicated behavior because of the onset of particle overshoot in which an excessively long time step is used to advect particles in a velocity field with strong small-scale gradients. We have shown that this effect leads to a reduction in particle trapping within coherent vortices, spuriously high particle dispersion, and a scrambling of Lagrangian diagnostics. A simple criterion for particle overshoot was formulated that provides for a given spatial resolution an estimate of the temporal resolution required to avoid overshoot. Although temporal interpolation and subgrid-scale models of the unresolved flow can, at a cost, ameliorate this effect, overshoot nonetheless places a potentially stringent restriction on the ability of raw altimetry velocity fields to accurately advect particles and fields.

We conclude that virtual tracer-based diagnostics are considerably more robust in turbulent flows with a steep submesoscale KE spectrum, whereas the applicability of these diagnostics to flows with an energized submesoscale should be viewed with some caution. Of the tracer-based diagnostics we consider, we find the absolute (or eddy) diffusivity to be the most robust to

undersampling in space and time. This is because the absolute diffusivity is governed by the slowly evolving large-scale modes, which are captured even at very low spatial and temporal resolution (Taylor 1921; Davis 1982). This is an encouraging result, because absolute diffusivity is the most straightforward diagnostic to incorporate into an ocean general circulation model. We anticipate that offline mixing studies using altimetric maps will continue to guide the development of more skillful parameterization schemes for oceanic mesoscale mixing.

Acknowledgments. This work was carried out with the support of a National Science Foundation “Collaborations in Mathematical Geosciences” Grant OCE-0620956. We also thank Banu Baydil and Darryn Waugh for their helpful input.

REFERENCES

- Abraham, E. R., and M. M. Bowen, 2002: Chaotic stirring by a mesoscale surface-ocean flow. *Chaos*, **12**, 373–381.
- , C. S. Law, P. W. Boyd, S. J. Lavender, M. T. Maldonado, and A. R. Bowie, 2000: Importance of stirring in the development of an iron-fertilized phytoplankton bloom. *Nature*, **407**, 727–730.
- Arbic, B., 2000: Generation of mid-ocean eddies: The local baroclinic instability hypothesis. Ph.D. thesis, Massachusetts Institute of Technology–Woods Hole Oceanographic Institute Joint Program, 293 pp.
- Babiano, A., C. Basdevant, and R. Sadourny, 1985: Structure functions and dispersion laws for two-dimensional turbulence. *J. Atmos. Sci.*, **42**, 941–949.
- , —, P. Le Roy, and R. Sadourny, 1990: Relative dispersion in two-dimensional turbulence. *J. Fluid Mech.*, **214**, 535–557.
- Bartello, P., 2000: Using low-resolution winds to deduce fine structure in tracers. *Atmos.–Ocean*, **38**, 303–320.
- Batchelor, G., 1952: Diffusion in a field of homogeneous turbulence. 2. The relative motion of particles. *Proc. Cambridge Philos. Soc.*, **48**, 345–362.
- Bennett, A., 1984: Relative dispersion: Local and nonlocal dynamics. *J. Atmos. Sci.*, **41**, 1881–1886.
- Berloff, P. S., and J. McWilliams, 2002: Material transport in oceanic gyres. Part II: Hierarchy of stochastic models. *J. Phys. Oceanogr.*, **32**, 797–830.
- , and —, 2003: Material transport in oceanic gyres. Part III: Randomized stochastic models. *J. Phys. Oceanogr.*, **33**, 1416–1445.
- , —, and A. Bracco, 2002: Material transport in oceanic gyres. Part I: Phenomenology. *J. Phys. Oceanogr.*, **32**, 764–796.
- Beron-Vera, F. J., M. J. Olascoaga, and G. J. Goni, 2008: Oceanic mesoscale eddies as revealed by Lagrangian coherent structures. *Geophys. Res. Lett.*, **35**, L12603, doi:10.1029/2008GL033957.
- Blumen, W., 1978: Uniform potential vorticity flow: Part I. Theory of wave interactions and two-dimensional turbulence. *J. Atmos. Sci.*, **35**, 774–783.
- Boffetta, G., A. Celani, M. Cencini, G. Lacorata, and A. Vulpiani, 2000: The predictability problem in systems with an uncertainty in the evolution law. *J. Phys.*, **33A**, 1313–1324.
- Bracco, A., J. von Hardenberg, A. Provenzale, J. Weiss, and J. McWilliams, 2004: Dispersion and mixing in quasigeostrophic turbulence. *Phys. Rev. Lett.*, **92**, 084501, doi:10.1103/PhysRevLett.92.084501.
- Charney, J., 1971: Geostrophic turbulence. *J. Atmos. Sci.*, **28**, 1087–1095.
- Conradsen, K., L. Nielsen, and L. Prahm, 1984: Review of Weibull statistics for estimation of wind speed distributions. *J. Climate Appl. Meteor.*, **23**, 1173–1183.
- Davis, R., 1982: On relating Eulerian and Lagrangian velocity statistics: Single particles in homogeneous flow. *J. Fluid Mech.*, **114**, 1–26.
- d’Ovidio, F., J. Isern-Fontanet, C. López, E. Hernández-García, and E. García-Ladona, 2009: Comparison between Eulerian diagnostics and finite-size Lyapunov exponents computed from altimetry in the Algerian basin. *Deep-Sea Res. I*, **56**, 15–31.
- Ducet, N., P. Le Traon, and G. Reverdin, 2000: Global high-resolution mapping of ocean circulation from TOPEX/Poseidon and ERS-1 and -2. *J. Geophys. Res.*, **105** (C8), 19 477–19 498.
- Durrant, D., 1999: *Numerical Methods for Wave Equations in Geophysical Fluid Dynamics*. Springer, 465 pp.
- Ferrari, R., and C. Wunsch, 2009: Ocean circulation kinetic energy: Reservoirs, sources, and sinks. *Annu. Rev. Fluid Mech.*, **41**, 253–282.
- Fu, L.-L., 2010: Determining ocean circulation and sea level from satellite altimetry: progress and challenges. *Oceans from Space*, V. Barale, J. Gower, and L. Alberotanza, Eds., Springer, 147–163.
- Griffa, A., 1996: Applications of stochastic particle models to oceanographic problems. *Stochastic Modeling in Physical Oceanography*, R. J. Adler, P. Muller, and B. L. Rozovskii, Eds., Birkhäuser Verlag, 114–140.
- , L. Piterbarg, and T. Özgökmen, 2004: Predictability of Lagrangian particle trajectories: Effects of smoothing of the underlying Eulerian flow. *J. Mar. Res.*, **62**, 1–35.
- Haidvogel, D. B., and I. Held, 1980: Homogeneous quasi-geostrophic turbulence driven by a uniform temperature gradient. *J. Atmos. Sci.*, **37**, 2644–2660.
- Hazell, D. R., and M. H. England, 2003: Prediction of the fate of radioactive material in the South Pacific Ocean using a global high-resolution ocean model. *J. Environ. Radioact.*, **65**, 329–355.
- Held, I., and V. Larichev, 1996: A scaling theory for horizontally homogeneous, baroclinically unstable flow on a beta plane. *J. Atmos. Sci.*, **53**, 946–952.
- , R. Pierrehumbert, S. Garner, and K. Swanson, 1995: Surface quasi-geostrophic dynamics. *J. Fluid Mech.*, **282**, 1–20.
- Isern-Fontanet, J., B. Chapron, G. Lepeyre, and P. Klein, 2006: Potential uses of microwave sea-surface temperatures for the estimation of ocean currents. *Geophys. Res. Lett.*, **33**, L24608, doi:10.1029/2006GL027801.
- Iudicone, D., G. Lacorata, V. Rupolo, R. Santoleri, and A. Vulpiani, 2002: Sensitivity of numerical tracer trajectories to uncertainties in OGCM velocity fields. *Ocean Modell.*, **4**, 313–325.
- Klein, P., B. L. Hua, G. Lapeyre, X. Capet, S. Le Gentil, and H. Sasaki, 2008: Upper-ocean turbulence from high-resolution 3D simulation. *J. Phys. Oceanogr.*, **38**, 1748–1763.
- Kraichnan, R., 1971: Inertial-range transfer in two- and three-dimensional turbulence. *J. Fluid Mech.*, **47**, 525–535.
- LaCasce, J., and C. Ohlmann, 2003: Relative dispersion at the surface of the Gulf of Mexico. *J. Mar. Res.*, **61**, 285–312.
- Lapeyre, G., and I. Held, 2003: Diffusivity, kinetic energy dissipation, and closure theories for the poleward eddy heat flux. *J. Atmos. Sci.*, **60**, 2907–2916.

- Lehahn, Y., F. d'Ovidio, M. Lévy, and E. Heifetz, 2007: Stirring of the northeast Atlantic spring bloom: A Lagrangian analysis based on multisatellite data. *J. Geophys. Res.*, **112**, C08005, doi:10.1029/2006JC003927.
- Le Traon, P., P. Klein, and B. L. Hua, 2008: Do altimeter wavenumber spectra agree with the interior or surface quasigeostrophic theory? *J. Phys. Oceanogr.*, **38**, 1137–1142.
- Lumpkin, R., and S. Elipot, 2010: Surface drifter pair spreading in the North Atlantic. *J. Geophys. Res.*, **115**, C12017, doi:10.1029/2010JC006338.
- Mahadevan, A., and J. W. Campbell, 2002: Biogeochemical patchiness at the sea surface. *Geophys. Res. Lett.*, **29**, 1926, doi:10.1029/2001GL014116.
- Majda, A. J., 1993: Explicit inertial range renormalization theory in a model for turbulent diffusion. *J. Stat. Phys.*, **73** (3–4), 515–542.
- , 1994: Random shearing direction models for isotropic turbulent diffusion. *J. Stat. Phys.*, **75** (5–6), 1153–1165.
- , and P. R. Kramer, 1999: Simplified models of turbulent diffusion: Theory, numerical modelling, and physical phenomena. *Phys. Rep.*, **314**, 237–574.
- , J. Harlim, and B. Gershgorin, 2010: Mathematical strategies for filtering turbulent dynamical systems. *Discrete Contin. Dyn. Syst.*, **27**, 441–486.
- Marshall, J., A. Adcroft, C. Hill, L. Perelman, and C. Heisey, 1997a: A finite-volume, incompressible Navier-Stokes model for studies of the ocean on parallel computers. *Geophys. Res. Lett.*, **102**, 5753–5766.
- , C. Hill, L. Perelman, and A. Adcroft, 1997b: Hydrostatic, quasi-hydrostatic, and nonhydrostatic ocean modeling. *J. Geophys. Res.*, **102** (C3), 5733–5752.
- , E. Shuckburgh, H. Jones, and C. Hill, 2006: Estimates and implications of surface eddy diffusivity in the Southern Ocean from tracer transport. *J. Phys. Oceanogr.*, **36**, 1806–1821.
- Martin, A., 2003: Phytoplankton patchiness: The role of lateral stirring and mixing. *Prog. Oceanogr.*, **57**, 125–174.
- Morel, P., and M. Larcheveque, 1974: Relative dispersion of constant-level balloons in the 200-mb general circulation. *J. Atmos. Sci.*, **31**, 2189–2196.
- Nakamura, N., 1996: Two-dimensional mixing, edge formation, and permeability diagnosed in an area coordinate. *J. Atmos. Sci.*, **53**, 1524–1537.
- , 2001: A new look at eddy diffusivity as a mixing diagnostic. *J. Atmos. Sci.*, **58**, 3685–3701.
- , 2008: Quantifying inhomogenous, instantaneous, irreversible transport using passive tracer field as a coordinate. *Transport and Mixing in Geophysical Flows*, J. B. Weiss and A. Provenzale, Eds., Vol. 744, *Lecture Notes in Physics*, Springer, 137–164.
- Ottino, J., 1990: Mixing, chaotic advection, and turbulence. *Annu. Rev. Fluid Mech.*, **22**, 207–253.
- Phillips, N., 1954: Energy transformations and meridional circulations associated with simple baroclinic waves in a two-level, quasigeostrophic model. *Tellus*, **6**, 273–286.
- Pierrehumbert, R., I. Held, and K. Swanson, 1994: Spectra of local and nonlocal two-dimensional turbulence. *Chaos Solitons Fractals*, **4**, 1111–1116.
- Piterburg, L. I., 2005: Relative dispersion in 2D stochastic flows. *J. Turbul.*, **6** (4), 1–19.
- Poje, A., A. Haza, T. Özgökmen, M. Magaldi, and Z. Garraffo, 2010: Resolution dependence of relative dispersion statistics in a hierarchy of ocean models. *Ocean Modell.*, **31** (1–2), 36–50.
- Richardson, L., 1926: Atmospheric diffusion shown on a distance-neighbour graph. *Proc. Roy. Soc. London*, **110A**, 709–737.
- Rossi, V., C. López, J. Sudre, E. Hernández-García, and V. Garçon, 2008: Comparative study of mixing and biological activity of the Benguela and Canary upwelling systems. *Geophys. Res. Lett.*, **35**, L11602, doi:10.1029/2008GL033610.
- Salmon, R., 1980: Baroclinic instability and geostrophic turbulence. *Geophys. Astrophys. Fluid Dyn.*, **15**, 167–211.
- Scott, R., and F. Wang, 2005: Direct evidence of an oceanic inverse kinetic energy cascade from satellite altimetry. *J. Phys. Oceanogr.*, **35**, 1650–1666.
- Shepherd, T., J. Koshyk, and K. Ngan, 2000: On the nature of large-scale mixing in the stratosphere and mesosphere. *J. Geophys. Res.*, **105** (D10), 12 433–12 446.
- Shuckburgh, E., and P. Haynes, 2003: Diagnosing transport and mixing using a tracer-based coordinate system. *Phys. Fluids*, **15**, 3342–3357.
- , H. Jones, J. Marshall, and C. Hill, 2009a: Robustness of effective diffusivity diagnostic in oceanic flows. *J. Phys. Oceanogr.*, **39**, 1993–2009.
- , —, —, and —, 2009b: Understanding the regional variability of eddy diffusivity in the Pacific sector of the Southern Ocean. *J. Phys. Oceanogr.*, **39**, 2011–2023.
- Smith, K., and G. Vallis, 2002: The scales and equilibration of midocean eddies: Forced-dissipative flow. *J. Phys. Oceanogr.*, **32**, 1699–1720.
- Stammer, D., 1997: Global characteristics of ocean variability estimated from regional TOPEX/Poseidon altimeter measurements. *J. Phys. Oceanogr.*, **27**, 1743–1769.
- Taylor, G., 1921: Diffusion by continuous movement. *Proc. London Math. Soc.*, **20**, 196–212.
- Tennekes, H., and J. Lumley, 1972: *A First Course in Turbulence*. MIT Press, 300 pp.
- Thompson, A., and W. Young, 2006: Scaling baroclinic eddy fluxes: Vorticity and energy balance. *J. Phys. Oceanogr.*, **36**, 720–738.
- Tulloch, R. T., and K. S. Smith, 2009: A note on the numerical representation of surface dynamics in quasigeostrophic turbulence: Application to the nonlinear Eady model. *J. Atmos. Sci.*, **66**, 1063–1068.
- Vallis, G., 2006: *Atmospheric and Ocean Fluid Dynamics: Fundamentals and Large-Scale Circulation*. Cambridge University Press, 745 pp.
- Waugh, D. W., and E. R. Abraham, 2008: Stirring in the global surface ocean. *Geophys. Res. Lett.*, **35**, L20605, doi:10.1029/2008GL035526.
- , —, and M. M. Bowen, 2006: Spatial variations of stirring in the surface ocean: A case study of the Tasman Sea. *J. Phys. Oceanogr.*, **36**, 526–542.